

Classifying Magnetosheath Jets using MMS - Statistical Properties

Savvas Raptis¹, Tomas Karlsson¹, Ferdinand Plaschke², Anita Kullen¹,
Per-Arne Lindqvist¹

¹Space and Plasma Physics, School of Electrical Engineering and Computer Science, KTH Royal Institute
of Technology, Stockholm, Sweden

²Space Research Institute, Austrian Academy of Sciences, Graz, Austria

Key Points:

- Classification of a jet database based on θ_{Bn} , using MMS magnetosheath data is presented.
- All classes show different properties with some classes being compatible with existent generation mechanisms.
- Bow shock ripple mechanism and SLAMS are generally supported by statistical properties.

Corresponding author: Savvas Raptis, savvra@kth.se

Abstract

Using Magnetospheric Multiscale (MMS) data, we find, classify and analyze transient dynamic pressure enhancements in the magnetosheath (jets) from May 2015 to May 2019. A classification algorithm is presented, using in-situ MMS data to classify jets ($N = 8499$) into different categories according to their associated angle between IMF and the bow shock normal vector (θ_{Bn}). Jets appearing for $\theta_{Bn} < 45$ are referred to as quasi-parallel, while jets appearing for $\theta_{Bn} > 45$ as quasi-perpendicular jets. Furthermore, we define those jets that occur at the boundaries between quasi-parallel and quasi-perpendicular magnetosheath as boundary jets. Finally, encapsulated jets are jet-like structures with similar characteristics to quasi-parallel jets while the surrounding plasma is of quasi-perpendicular nature.

We present the first statistical results of such a classification and provide comparative statistics for each class. Furthermore, we investigate correlations between jet quantities. Quasi-parallel jets have the highest dynamic pressure while occurring more often than quasi-perpendicular jets. The infrequent quasi-perpendicular jets, have a much smaller duration, velocity, and density and are therefore relatively weaker. We conclude that quasi-parallel and boundary jets have similar properties and are unlikely to originate from different generation mechanisms. Regarding the encapsulated jets, we suggest that they are a special subset of quasi-parallel jets originating from the flanks of the bow shock, for large IMF cone angles although a relation to FTEs and magnetospheric plasma is also possible. Our results support existing generation theories, such as the bow shock ripple and SLAMS-associated mechanisms while indicating that other factors may contribute as well.

1 Introduction

The magnetosheath plasma can have strong fluctuations in velocity, density, and associated magnetic field. A key component that influences the level of fluctuation is the angle between the IMF and the bow shock normal vector (θ_{Bn}). It has been shown that in the case of the quasi-parallel shock ($\theta_{Bn} < 45$) the downstream plasma is strongly turbulent whereas in the quasi-perpendicular shock ($\theta_{Bn} > 45$) there is a much smoother and calmer environment (Fuselier, 2013; Wilson III, 2016). The main reason the two regions have different characteristics is that in the quasi-parallel case, reflected ions can travel upstream along the magnetic field lines causing instabilities, and associated wave growth. This creates a foreshock region characterized by a suprathermal ion distribution. This region is not present in the quasi-perpendicular case where the transition between upstream and downstream flow is distinct and straightforward (Schwartz & Burgess, 1991). As a result, in the quasi-perpendicular bow shock, there are much sharper and well-defined transitions between the upstream and downstream plasma.

Magnetosheath jets are local enhancements of dynamic pressure above the surrounding background level, reaching values even higher than the upstream solar wind. The dynamic pressure enhancements can be attributed to a density increase (Savin et al., 2008; Karlsson et al., 2012, 2015), a velocity increase (Archer et al., 2012) or may result from an enhancement of both (Amata et al., 2011; Plaschke et al., 2013). These jets are mainly found downstream of the quasi-parallel bow shock and the current prominent formation theory is that they result from foreshock fluctuations interacting with the bow shock.

Many terms and definitions have been used in the literature to describe the jet phenomenon, as thoroughly discussed in the review paper by Plaschke et al. (2018). In principle, the jet determination can be done via two methods. The first one is by using a sliding average time window which indicates a background value on the magnetosheath dynamic pressure and searches for enhancements that are 100% - 200% higher than that value. (Archer & Horbury, 2013; Gunell et al., 2014; Karlsson et al., 2015; Gutynska et al., 2015). Another way is to apply a minimum threshold to the x component of the dy-

66 namic pressure to be at least 25% of the solar wind’s associated dynamic pressure (Amata
 67 et al., 2011; Hietala et al., 2012; Plaschke et al., 2013). In this work we will use the term
 68 ”magnetosheath jet” or ”jet” to describe an enhancement in the dynamic pressure com-
 69 pared to the values of the background magnetosheath plasma, using a sliding time win-
 70 dow.

71 The dynamic pressure enhancements can reach up to ~ 15 times of the background
 72 value. Their duration can be of the order of seconds, up to several minutes with an av-
 73 erage of 30 seconds (Archer & Horbury, 2013). Parallel to the flow, the scale is ~ 0.5
 74 R_E and in the perpendicular direction slightly more at roughly $\sim 1 R_E$ (Archer & Hor-
 75 bury, 2013; Plaschke et al., 2018). While as mentioned above, jets’ dynamic pressure en-
 76 hancement is usually attributed to both density and velocity increase (Amata et al., 2011;
 77 Archer & Horbury, 2013), there are cases where some jets exhibit a density decrease. Specif-
 78 ically, Plaschke et al. (2013), found 10.5% of jets showing a density decrease. On the other
 79 hand, Archer et al. (2012) using a different jet criterion found up to 18% of jets exhibit-
 80 ing a density drop. Furthermore, jets can generate a vortical motion in the background
 81 magnetosheath plasma, causing a deceleration to the ambient plasma around the jet (Plaschke
 82 & Hietala, 2018). It has been recently shown that jets occur roughly 9 times more of-
 83 ten downstream of the quasi-parallel bow shock compared to the quasi-perpendicular one
 84 (Vuorinen et al., 2019). This is in agreement with the observations showing low solar wind
 85 cone angles favoring the formation of subsolar magnetosheath jets, while other solar wind
 86 parameter variations have no significant effect (Plaschke et al., 2013).

87 Magnetosheath jets may have an important impact on the magnetosphere. Their
 88 increased momentum can create local deformation of the magnetopause and trigger lo-
 89 cal magnetic reconnection (Hietala et al., 2018), drive compressional waves (Plaschke &
 90 Glassmeier, 2011) or even cause direct plasma penetration in the magnetosphere (Karlsson
 91 et al., 2012; Dmitriev & Suvorova, 2015). Furthermore, they can affect the radiation belts
 92 through the loss of outer belt electrons, (Turner et al., 2012; Xiang et al., 2016). Addi-
 93 tionally, jets can cause aurora brightening through the compression of the magnetosphere
 94 (Wang et al., 2018) or can affect the aurora via the mechanism of ”dayside throat au-
 95 rora” which has been connected to magnetosheath particle precipitation (Han et al., 2017).
 96 The link between jets and energy transfer through the magnetosphere was also observed
 97 recently when surface eigenmodes were found to be excited through a collision between
 98 a jet and the magnetopause (Archer et al., 2019). Finally, jets seem to be a universal
 99 phenomenon that is speculated to occur in other planetary and astrophysical bow shocks
 100 (Giacalone & Jokipii, 2007; Plaschke et al., 2018).

101 1.1 Generation of jets

102 While the generation of jets is not yet fully explained, a prominent theory is that
 103 the majority of the jets are associated with ripples of the quasi-parallel bow shock. Hietala
 104 et al. (2009) and Hietala and Plaschke (2013) propose that through the interaction with
 105 a locally curved bow shock, plasma flows are less decelerated while still being compressed.
 106 This results in a relative velocity difference compared to the surrounding flow that gets
 107 more decelerated, explaining the dynamic pressure enhancement (”jet”) observed in the
 108 magnetosheath region. A similar mechanism, where foreshock short large-amplitude mag-
 109 netic structures (SLAMS) interact with the local bow shock ripples may be responsible
 110 for generating some jets. SLAMS (upstream pulsations) are typical phenomena in the
 111 quasi-parallel foreshock and have very large magnetic field amplitudes (~ 5 times higher
 112 than the background) (Schwartz et al., 1992). Regarding jets, it has been suggested that
 113 jets associated with SLAMS can have a relative increase of density and magnetic field
 114 strength whereas the ones associated with purely bow shock ripple mechanism may be
 115 mainly velocity driven (Karlsson et al., 2015). Furthermore, there have been recent sim-
 116 ulations supporting the generation of a SLAMS-like subset of jets (Palmroth et al., 2018).

117 Another theory associates the formation of jet-like transient phenomena with IMF
 118 rotational discontinuities. Early simulations have shown that pressure pulses may be gen-
 119 erated when there is a switch between quasi-perpendicular and quasi-parallel bow shock
 120 or vice versa (Lin et al., 1996). Later, Dmitriev and Suvorova (2012) reported evidence
 121 of a jet, generated by a rotational discontinuity. Archer et al. (2012) found several jets
 122 that were consistent with this picture by using upstream and downstream solar wind data
 123 while Karlsson et al. (2018) investigated the anatomy of some typical cases that exhibit
 124 a magnetic field rotation in the magnetosheath.

125 Additional mechanisms have been suggested, involving solar wind discontinuity-
 126 related hot flow anomalies (HFAs) which can act as an obstacle to the upstream solar
 127 wind flow (Savin et al., 2012). Another possible mechanism relates jets to the sponta-
 128 neous hot flow anomalies (SHFAs) resulting from foreshock cavitons (Zhang et al., 2013;
 129 Omidì et al., 2013). Retinò et al. (2007), connected magnetic reconnection inside the mag-
 130 netosheath with local particle acceleration which could appear as jets. This mechanism,
 131 however, is not sufficient to explain jets with velocities much greater than the local Alfvén
 132 speed (Archer et al., 2012). Other proposed mechanisms describe the jet phenomenon
 133 in terms of a slingshot effect (Chen et al., 1993; Lavraud et al., 2007). This effect attributes
 134 the velocity enhancement of jets to a release of magnetic tension of a flux tube along the
 135 flanks.

136 There is no consensus regarding which of the above theories is responsible for the
 137 origin of jets. Furthermore, there has been no investigation regarding statistical differ-
 138 ences that may arise in the properties of the jets depending on the angle between the
 139 IMF field and the bow shock normal vector. In this work, we address both of these knowl-
 140 edge gaps by defining different classes of jets and investigating their statistical proper-
 141 ties to give insight into how likely each generation mechanism is for each class.

142 1.2 Different Types of Jets

143 Using MMS data we identify and classify the jets into 4 main categories. Jets have
 144 been observed for over 20 years now downstream of the quasi-parallel bow shock (Němeček
 145 et al., 1998). It is believed that the majority of jets are occurring in a quasi-parallel con-
 146 figuration and therefore the first category we search for are the "Quasi-parallel (Qpar)
 147 jets". As a complementary category, we are investigating cases of jets that are downstream
 148 of the quasi-perpendicular bow shock that we call "Quasi-perpendicular (Qperp) jets".
 149 Furthermore, we classified jets that are found at the boundary between a Qpar and a
 150 Qperp geometry or vice versa. Our goal is to investigate if these jets are connected to
 151 the mechanism proposed by Archer et al. (2012), and we call them "Boundary jets". It
 152 has been hypothesized that maybe these jets are different than the other classes and may
 153 hold separate properties (Archer et al., 2012; Archer & Horbury, 2013; Karlsson et al.,
 154 2018). Finally, after inspecting the derived dataset, we introduce a category called "En-
 155 capsulated jets". These jets contain plasma with very similar characteristics to Qpar, while
 156 the surrounding plasma is of Qperp nature.

157 Apart from the main categories, in the jet database, we include 2 more classes. The
 158 first are the ones that were identified as jets but were not classified by the algorithm by
 159 not fulfilling all necessary criteria. These jets, therefore, remain as 'Unclassified jets' un-
 160 til further inspection. Secondly, jets found very close to either the bow shock or the mag-
 161 netopause ('Border jets') are not investigated in this work to exclude possible edge ef-
 162 fects. The main goal of this work is to investigate the statistical properties and the dif-
 163 ferences between these classes. As a result, the goal of the classification procedure is to
 164 derive enough samples to provide meaningful comparison and not to provide a class for
 165 every observed event. This was done in order to minimize misclassification and to only
 166 have very clear cases for each class.

167 2 Data

168 In this study, we use data starting from the 1st of September 2015 until the 1st
 169 of May 2019. For the measurements that characterize the jets in the magnetosheath, we
 170 use data from the MMS (Magnetospheric Multiscale) mission (Burch et al., 2016), while
 171 for the upstream values of the solar wind we use data primarily from the ACE (Advanced
 172 Composition Explorer) mission (Stone et al., 1998a). The measurements used for both
 173 solar wind and magnetosheath regions are presented in Geocentric Solar Ecliptic (GSE)
 174 coordinates.

175 2.1 MMS - Magnetosheath Data

176 For magnetic field measurements, we use the fluxgate magnetometer (FGM) (Russell
 177 et al., 2016) which has a resolution of 1/0.125 sample/sec in the slow survey mode. Fur-
 178 thermore, we use the fast plasma investigation (FPI) (Pollock et al., 2016) which has a
 179 time resolution of 4.5 seconds for ion measurements. Finally, for determining the posi-
 180 tion of MMS, the Magnetic Ephemeris Coordinates (MEC) data that are included in the
 181 MMS dataset are used (Burch et al., 2016).

182 During their orbit, the MMS spacecraft are regularly traversing the magnetosheath
 183 region. The small separation of the four MMS spacecraft allows us to only use data from
 184 MMS1 for the purposes of this paper.

185 2.2 OMNIweb/ACE - Solar Wind Data

186 For parts of the analysis, we use upstream solar wind measurements, publicly avail-
 187 able through the 1-minute resolution OMNI database. This dataset is created using mul-
 188 tiple spacecraft measurements (primarily ACE & Wind (Stone et al., 1998b)) and is smoothed
 189 and time-shifted to the nose of the Earth’s bow shock. The bow shock location changes
 190 according to the solar wind parameters and is automatically adjusted for every time-shifted
 191 measurement (King & Papitashvili, 2005). The time resolution of the OMNIweb high-
 192 resolution database is 1 data point per minute. To associate OMNIweb data to the jets
 193 we took average solar wind values of a 15-minute window, starting 10 minutes before the
 194 jet’s observation time and up to 5 minutes after. This value seemed to provide accurate
 195 results in the cases that we tested manually, and was done to compensate for several pos-
 196 sible errors that are explicitly analyzed in the method section below. As a result, every
 197 jet that has been measured by MMS in the magnetosheath is associated to average solar
 198 wind quantities from the OMNIweb database.

199 3 Method

200 3.1 Magnetosheath Identification

201 The determination of each region (magnetosheath/solar wind/magnetosphere) is
 202 done based on manually derived thresholds for ion number density (n_i), velocity (V_i),
 203 temperature (T_i), and differential energy flux of high-energy ions (F_i). Furthermore, we
 204 require three (3) sequential data points to be classified as a different region in order to
 205 change the region’s characterization (e.g. transitioning from the magnetosheath to the
 206 solar wind). This was done to avoid cases where due to the variance of the measurements,
 207 one point might be misclassified as another region. Finally, we impose a minimum du-
 208 ration for each region to be 15 minutes. Smaller regions were considered to be possibly
 209 influenced by bow shock or magnetopause crossings.

Table 1. Initial dataset of the magnetosheath jets for the period 10/2015 - 04/2019.

Subset	Number (n)	Percentage (%)	Criteria
All	16034	100	Eq. (1)
Combined	8499	53	Eqs. (1), (3)

3.2 Jet Determination

For jet determination, we rely only on local magnetosheath data. Doing so, we increase the dataset sample size by not limiting observations to time periods where upstream solar wind data are available. We found that roughly $\sim 27\%$ of the jets contained missing data in their corresponding solar wind dynamic pressure. As a result, the choice of local MMS measurements for jet determination appears to be superior regarding the size of the derived dataset.

For the initial dataset, we impose a minimum relative dynamic pressure threshold, which defines a jet as the time interval in which the dynamic pressure is at least twice as large as a 20-min average value. Specifically, we use:

$$P_{msh} \geq 2\langle P_{msh} \rangle_{20 \text{ min}} \quad (1)$$

where,

$$P_{msh} = m_p n_i V_i^2 \quad (2)$$

and angular brackets denote an averaging by a 20 min sliding window. When magnetosheath regions are less than 20 minutes, the average window is taken to be equal to the available region. The choice of this criterion was primarily done to compare with other statistical works done with a similar criterion (e.g. (Archer et al., 2012)). Furthermore, criteria using solar wind values were avoided since the presented work contains jets occurring at the flanks of the magnetosheath, and such criteria would be met all the time.

We then implement an additional criterion, combining all the jets that have a shorter time separation than 60 seconds from each other.

$$t_{start,i+1} - t_{end,i} \geq 60\text{s} \quad (3)$$

Where $i = 1, 2, 3 \dots n$ is the number of the jet in the database.

This was done based on the assumption that jets with such a small time separation are part of the same fast plasma flow. A similar technique is also applied when studying flows that occur in the plasma sheet, known as bursty bulk flows (BBFs) (Angelopoulos et al., 1994). Furthermore, not combining jets may lead to skewed statistics since it can result in an artificially increased number of jets with much shorter duration and similar properties, possibly causing misleading results.

After obtaining the jet dataset, as shown in Table 1, we implement an automatic classification algorithm to create a subset of jets for each class. The algorithm includes 5 stages of classification that are implemented sequentially. The purpose of this method is to increase the number of jets that are classified after every stage while only slightly increasing the misclassification cases. In the following subsections, we will briefly explain

Table 2. Properties of the four main classes of jets.

Name	Characteristics
Quasi-parallel	High energy ion flux, low ion temperature anisotropy, high magnetic field variance
Quasi-perpendicular	Low energy ion flux, high ion temperature anisotropy, low magnetic field variance
Boundary	Switch between Qpar characteristics to Qperp or Vice Versa
Encapsulated	Switch from Qperp characteristics to Qpar and back to Qperp

241 some key ideas and components of the algorithm, while more details can be found in Ap-
 242 pendix A, Appendix B and in the supplementary material.

243 3.3 Jet Classification

244 For the jet classification, we only use MMS data. Similar to the jet determination
 245 algorithm, the classification code avoids the use of solar wind measurements. This was
 246 done for several reasons. The solar wind values available are measured at L_1 and are time-
 247 lagged, introducing an error from the artificial propagation to the bow shock nose. The
 248 generated error in such a time-lagging procedure can reach values up to 30 minutes (Mailyan
 249 et al., 2008; Case & Wild, 2012), while producing large uncertainty in short time scale
 250 phenomena (e.g. rotations of magnetic field). Furthermore, the available measurements
 251 are averaged to 1 minute, which makes certain short time scale features impossible to
 252 detect. Additionally, the jets are identified throughout the whole magnetosheath region,
 253 meaning that one has to time-shift the associated solar wind values after the bow shock
 254 interaction, differently for each jet, in order to accurately characterize the jets, provid-
 255 ing additional uncertainty to the measurements. Finally, for roughly 1/4 of the jets IMF
 256 measurements were not available for a sufficiently long period of time to accurately clas-
 257 sify them. All the above reasons led us to primarily use magnetosheath data rather than
 258 solar wind for the classification.

259 It has been shown that the quasi-parallel (Qpar) magnetosheath has different prop-
 260 erties than the quasi-perpendicular (Qperp) magnetosheath. Specifically, in Qpar mag-
 261 netosheath, temperature anisotropy is typically different compared to the Qperp one (Anderson
 262 et al., 1994; Fuselier et al., 1994). Furthermore, stronger fluctuations in the plasma den-
 263 sity, velocity, and the magnetic field have been associated with Qpar magnetosheath (Formisano
 264 & Hedgecock, 1973; Luhmann et al., 1986). Finally, the most striking difference is a dis-
 265 tinct high energy ion population that can be observed in the Qpar magnetosheath (Gosling
 266 et al., 1978; Fuselier, 2013). Therefore, the classification code works by applying man-
 267 ually derived thresholds to the ion energy flux, temperature anisotropy and, magnetic
 268 field standard deviation. The quantities used for the classification are discussed later,
 269 while the values for each threshold are provided in Appendix A.

270 The characteristics of the 4 main classes of jets are summarized in Table 2.

271 In order to verify that we can accurately distinguish between Qpar and Qperp mag-
 272 netosheath, we checked the measurements of MMS when it was close to the subsolar point
 273 of the bow shock. Due to the proximity to the subsolar point, there is a smaller error
 274 in the propagation of the solar wind measurements to the bow shock, and a shorter dis-
 275 tance for the plasma flow to propagate inside the magnetosheath. Therefore, we can con-
 276 firm the expected characteristics of the magnetosheath plasma. An example of such a
 277 test can be seen in Figure 1. The cone angle is defined as:

$$\theta_{cone} = \arccos\left(\frac{|B_x|}{|B|}\right) \quad (4)$$

278 which in the case of subsolar point it is identical to θ_{Bn} since the bow shock normal vec-
 279 tor \hat{n} is pointing in the x direction.

280 As shown in Figure 1, there are distinct magnetosheath characteristics associated
 281 with the quasi-parallel and quasi-perpendicular bow shock. The high energy ion flux
 282 is the one that is most noticeable, while the ion temperature anisotropy, and the magnetic
 283 field variance are also correlated with the change of the cone angle. The exact compu-
 284 tation of these quantities can be found in Appendix A. Interestingly, the region which
 285 is not shaded with any color is a typical example where the high resolution measurements
 286 of MMS provide evidence of a short-time scale change of IMF while the cone angle mea-
 287 surements of 1-min resolution fully miss the rapid change that is seen in the magnetosheath.
 288 The purpose of this example is to verify that the classification of jets into Qpar and Qperp
 289 can be performed using only local MMS measurements by comparing with a proxy for
 290 θ_{Bn} . MMS1 is located at $(11.37, -0.02, -1.01)R_E$ in GSE coordinates. This position was
 291 chosen to be close to the subsolar region. This was done to minimize the difference be-
 292 tween θ_{cone} and θ_{Bn} while limiting the time-shift effect from the bow shock to MMS po-
 293 sition.

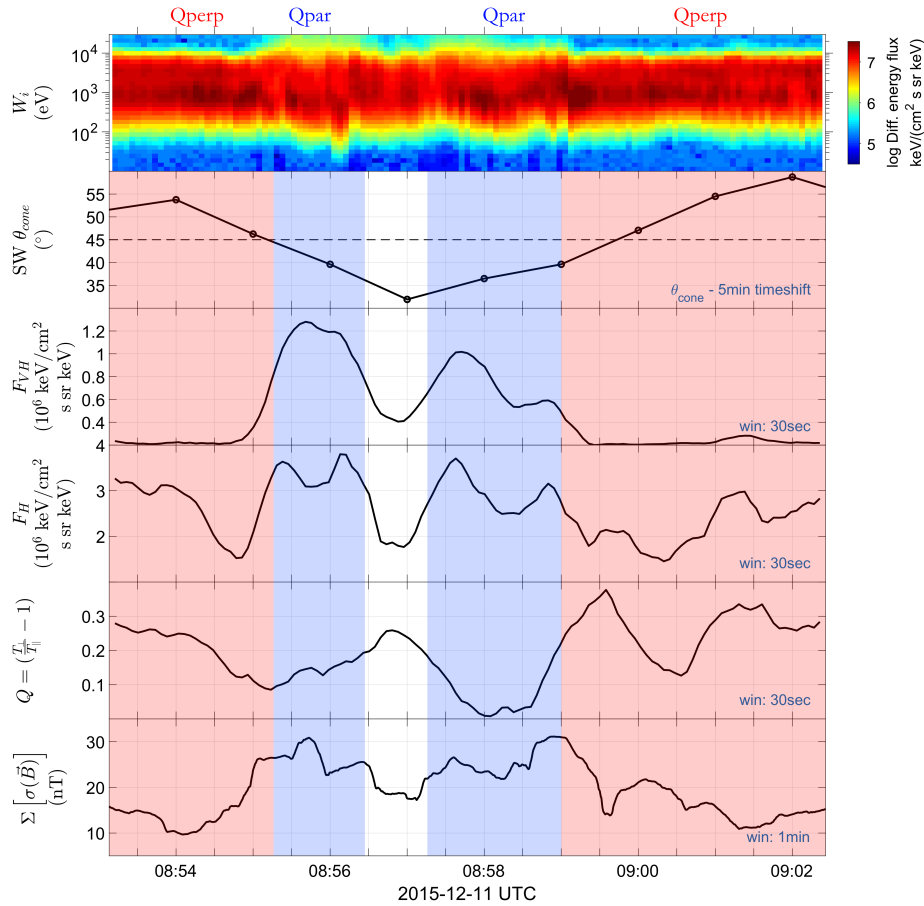


Figure 1. Visualization of associated changes between Qpar and Qperp magnetosheath. From top to bottom, ion energy spectrogram, solar wind cone angle, very high energy (16 – 28 keV) averaged differential ion flux, high energy (7 – 12 keV) averaged differential ion flux, ion temperature anisotropy, and sum of the magnetic field standard deviation. Blue shaded region represent Qpar regions while red show Qperp ones. More information about the computation of each quantity can be found in Appendix A.

294 Typical examples of each jet class can be seen in Figure 2. In Figure 2(a), we show
 295 a quasi-parallel jet whereas in Figure 2(b) a quasi-perpendicular one. A boundary jet
 296 can be seen in Figure 2(c) and finally an encapsulated one in Figure 2(d).

297 **3.3.1 Pre-jet and Post-jet Periods**

298 The classification scheme is based on the assumption that there are three distinct
 299 phases in the jet phenomenon. Since the jet crosses MMS, observations include the plasma
 300 environment propagating in front of the jet, the jet flow and the plasma behind the jet.
 301 These plasma environments are called, pre-jet, jet and post-jet periods, respectively.

302 The jet period is the duration in which the criterion of Eq. (1) is satisfied. In the
 303 case that the jet contains only one data point ($\sim 30\%$), we re-adjust the starting and
 304 ending point of the jet to include one extra data point before and after the jet respec-
 305 tively. The pre-jet period is a period of time before the actual jet which is usually char-
 306 acterized by a gradual increase in dynamic pressure. The post-jet period is an equally
 307 long period of time, characterized by a gradual drop of dynamic pressure associated with
 308 a non-jet magnetosheath region.

309 The pre/post-jet time periods are set based on jet duration as:

$$\Delta t_{\text{pre,post}} = \begin{cases} 45 \text{ sec}, & \Delta t_{\text{jet}} < 45 \text{ sec} \\ 60 \text{ sec}, & 45 \text{ sec} \leq \Delta t_{\text{jet}} < 75 \text{ sec} \\ 75 \text{ sec}, & \Delta t_{\text{jet}} \geq 75 \text{ sec} . \end{cases} \quad (5)$$

310 It was decided to have the pre/post jet time increasing with jet duration mainly
 311 to assist the classification routine which is categorizing data points and chooses the class
 312 of each jet based on the percentage of them that fit the classification criteria. Further-
 313 more, by manually inspecting cases of extensive duration jets ($\Delta t_{\text{jet}} > 45 \text{ sec}$) we found
 314 that a slight increase to their pre/post jet times made the classification algorithm more
 315 accurate.

316 **3.3.2 Verification and Validation of Data Set**

317 In order to determine the settings for the classification scheme, a test data set was
 318 created through visual inspection, containing jets of every class. After testing the ac-
 319 curacy of our classification procedure the best stage from which the output was sufficient
 320 to derive statistical results was chosen (Appendix B).

321 As a final validation, a visual inspection accompanied by a manual reclassification
 322 was made for a few misclassifications that the automatic procedure produced ($\sim 10\text{--}$
 323 20%). This resulted in some slight changes to the dataset while ensuring that the accu-
 324 racy of the classification is satisfactory. Typically, the majority of automatic misclas-
 325 sifications were found in the boundary and encapsulated cases. This was expected since
 326 these classes had much more precise criteria to be met both in the jet and in the sur-
 327 rounding plasma region. More information regarding the verification of the data set and
 328 the accuracy determination of the procedure can be found in Appendix B and in the sup-
 329plementary material.

330 The number of jets in the final classified dataset is shown in Table 3.

331 The position for all the main class jets is shown in Figure 3. There, the MMS posi-
 332 tion at the time of observation of the maximum dynamic pressure is shown. The mag-
 333 netopause and bow shock regions are plotted based on the model found in Chao et al.
 334 (2002) and by using the average solar wind conditions that were found for all the jets
 335 in the dataset. In particular, the model used here and below uses the following quan-

Table 3. Classified dataset of the magnetosheath jets for the period 09/2015 - 04/2019. Using as initial dataset the combined ($N = 8499$) jets of Table 1. The properties of each class are shown in Table 2.

Subset	Number	Percentage (%)
Quasi-parallel	2284	26.9
Final cases	860	10.1
Quasi-perpendicular	504	5.9
Final cases	211	2.5
Boundary	744	8.8
Final cases	154	1.8
Encapsulated	77	0.9
Final cases	57	0.7
Other	4890	57.5
Unclassified/Uncertain	3499	41.2
Border	1346	15.8
Data Gap	45	0.5

336 titles. For the magnetopause model, the model uses the z-component of the interplan-
 337 etary magnetic field (B_z) and the ion dynamic pressure (P_{dyn}). In addition, the bow shock
 338 model also uses the magnetosonic Mach number (\mathcal{M}_{ms}) and the beta plasma parameter
 339 (β). For the average model shown in Figure 3, the conditions used are, $B_z = -0.075$
 340 (nT), $P_{dyn} = 2.07$ (nPa), $\mathcal{M}_{ms} = 5.97$ and $\beta = 2.45$.

341 3.4 Derived quantities

342 In order to derive statistical results for each of the classes, the "final cases" listed
 343 in Table 3 are used. These jets met all necessary criteria from the automatic procedure
 344 and have also been manually verified. As a result, unless explicitly mentioned, we use
 345 the verified ("final") cases for our analysis. Finally, when we are referring to "main" classes
 346 we mean the four classes described in Table 2. More information regarding the criteria
 347 and the exact determination of these cases are given in the appendices (Appendix A and
 348 Appendix B) of this article and in the supplementary material.

349 For all the jets, different variations of the minimum, mean and maximum values
 350 of their properties are investigated. Most importantly, an analysis on how these quan-
 351 tities are distributed compared to the background magnetosheath plasma is being done.
 352 This analysis is conducted by introducing "difference" values, referring to quantities that
 353 are either maximum, mean, or minimum within a jet from which a 5-minute background
 354 magnetosheath value is subtracted.

$$\Delta X_{(max/mean/min,5)} = X_{max/mean/min} - \langle X \rangle_{MSH}. \quad (6)$$

355 In the background value ($\langle X \rangle_{MSH}$), we remove the jet period. As a result,

$$\langle X \rangle_{MSH} = \frac{1}{2n} \sum_i^n (X_{t_{start}-i} + X_{t_{end}+i}) \quad (7)$$

356 where start/end is the starting and ending point of the jet period, and $n = 33$ measure-
 357 ments.

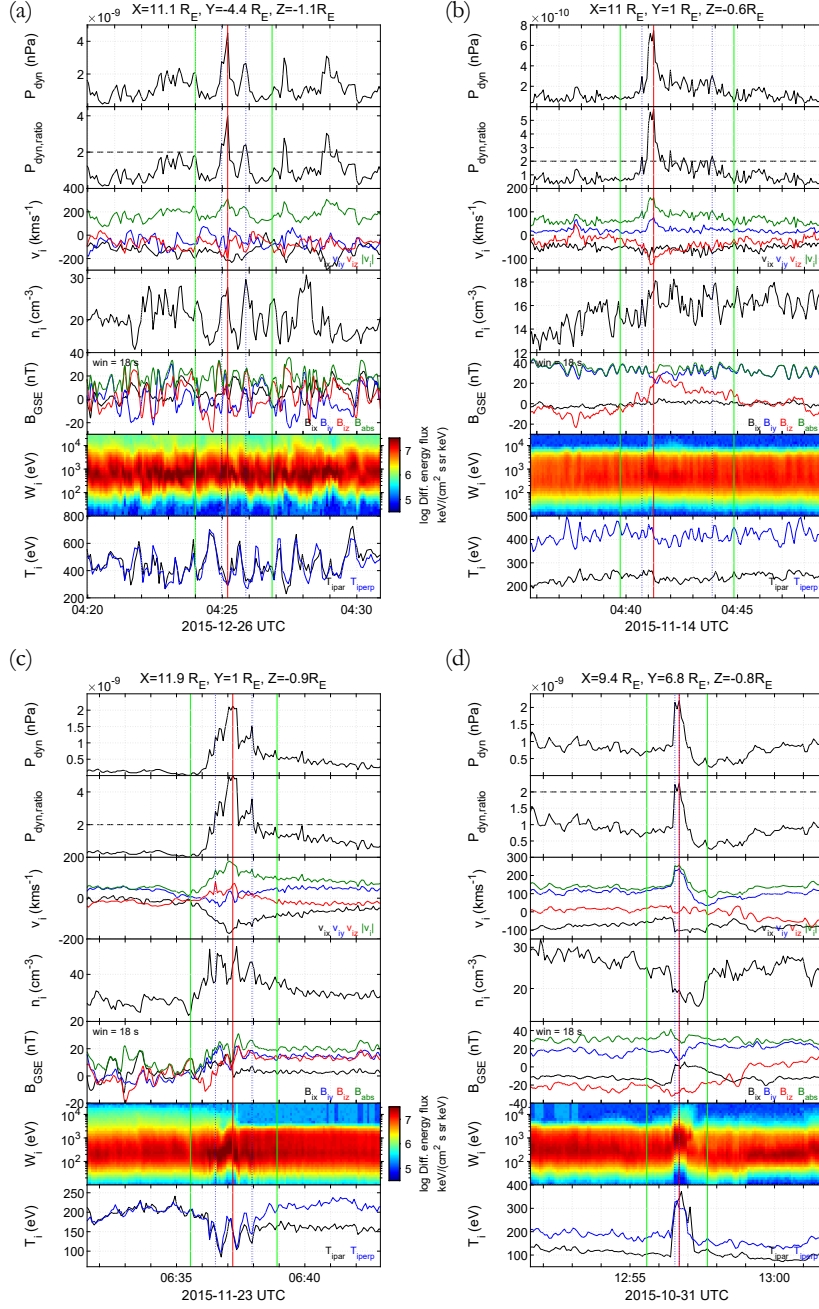


Figure 2. Examples of the four main categories of jets. (a): Quasi-parallel, (b): Quasi-perpendicular, (c): Boundary, and (d): Encapsulated jet. From top to bottom, in each subplot: dynamic pressure, ratio of the dynamic pressure to the background level, ion velocity, ion number density, magnetic field components averaged with a moving window of 18 seconds, ion energy spectrum and parallel and perpendicular components of ion temperature. The red vertical line shows the time of maximum dynamic pressure, blue vertical lines the jet period, and green vertical lines indicate the pre-jet and post-jet times. Finally, the black dotted line on the second panel of every subplot indicates a 200% enhancement of dynamic pressure compared to the background.

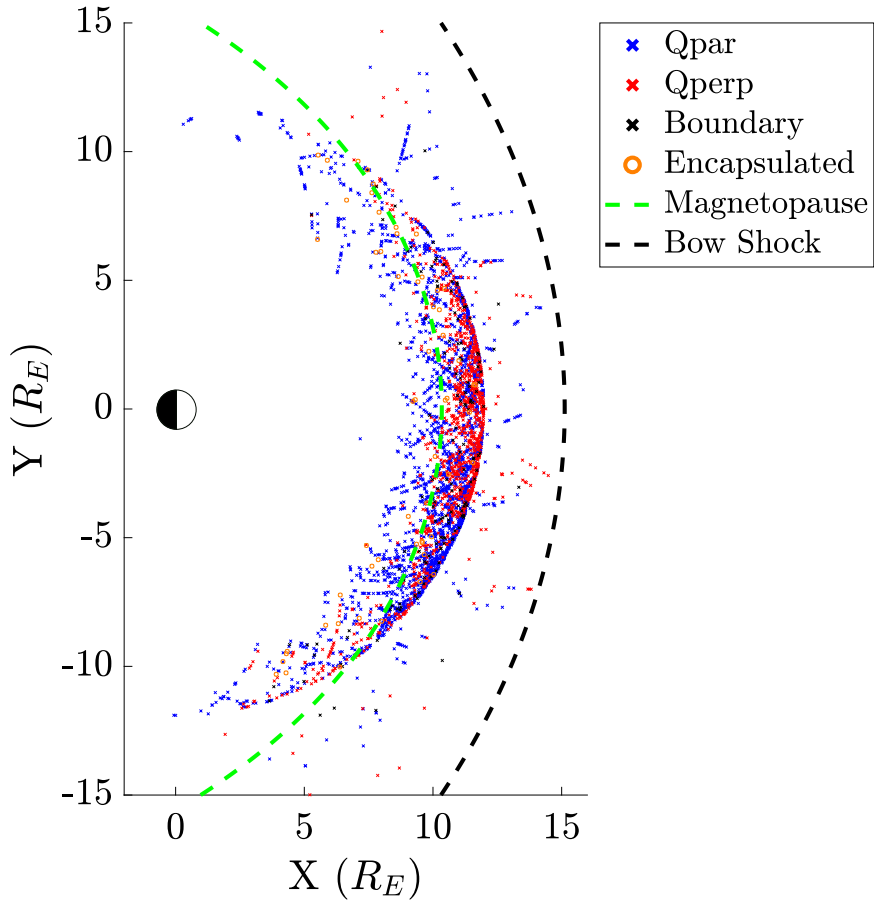


Figure 3. Location of the 4 magnetosheath jet classes projected to the xy -plane in GSE coordinates, identified in MMS data between May 2015 and May 2019. The green and black dashed lines mark the approximate location of the magnetopause and the bow shock during solar wind conditions averaged over the periods that a jet was found. Coordinate system is the Geocentric Solar Ecliptic (GSE) and both axes are normalized to Earth radius ($R_E = 6.371$ km).

358 The differences between the mean and max values were, statistically speaking, in-
 359 significant due to the short duration of the jets. Therefore, in order to make the visu-
 360 alization easier, the maximum values are primarily shown. It should be noted that the
 361 "difference" values (Eq. (6)) can give insight in the cases of Qpar and Qperp jets but
 362 should be treated with caution when referring to the boundary and encapsulated jets.
 363 The reason is that the background normalization in the first two cases is being done with
 364 plasma which is more or less similar throughout the 5 minute period that was taken. On
 365 the other hand, for the boundary and encapsulated cases, due to the nature of plasma
 366 being different between the jet and the surrounding measurements, the difference val-
 367 ues can be unreliable.

368 To determine the distance of each jet from the bow shock, a model for every jet
 369 based on its associated solar wind values was generated. The average associated solar
 370 wind conditions are derived from values 10 min before the jet and up to 5 minutes af-
 371 ter. The asymmetric usage of measurements before and after the jet was done to com-
 372 pensate for the time plasma takes to travel from the bow shock to the MMS position.

373 Later, the maximum velocity vector (\mathbf{V}_{max}) of each jet was used to propagate it back
 374 in time until a bow shock crossing was found. This procedure took ΔT_{BS_i} time for each
 375 jet (i) which was calculated as the number of steps multiplied by the time resolution of
 376 the FPI instrument (4.5 seconds). After approximating a point of origin for each jet, the
 377 distance from the bow shock is computed as:

$$\Delta X_{BS} = X_{BS} - X_{MMS} \quad (8)$$

378 where X can be radial distance (R), distance along the yz plane (ρ), or distance along
 379 the x axis (X). It should be noted, that the modeled position of the bow shock may have
 380 a significant error as shown in several studies (e.g. (Merka et al., 2003; Turc et al., 2013))
 381 and therefore any statistical results should be considered with caution.

382 Furthermore, the algorithm which computed the point of origin for each jet, assumes
 383 that no breaking nor change in the direction of the jet occurred from its creation until
 384 its observation by MMS. This assumption is certainly not ideal and it produced some
 385 cases where the jet was found to originate from a non-physical origin (e.g. $\Delta R > 30$
 386 R_E). In these cases, we used the dominant component of the velocity to propagate the
 387 jet to the bow shock as an alternative option. However, there were cases that still pro-
 388 vided unphysical results. An algorithm identified these cases by checking whether the
 389 origin was extremely far away from the position the jet was found or if the time it took
 390 a jet to reach the bow shock was more than 30 minutes. In these cases, we simply re-
 391 moved the jet from this specific analysis. This procedure reduced the number of jets in
 392 all classes slightly. Specifically, 4 Qpar, 2 Qperp, 2 boundary, and 1 encapsulated jets
 393 were removed.

394 Similarly, a magnetopause model was generated using the model by Chao et al. (2002)
 395 and the solar wind conditions at the time of each jet observation. The magnetopause model,
 396 while also prone to several errors, can provide vital information regarding the relative
 397 position of jets of different classes. After, modeling the magnetopause for each jet, the
 398 radial distance from the closest point was measured as

$$\Delta R_{MP} = R_{MP} - R_{MMS} \quad (9)$$

399 where, R_{MP} is the closest point of the magnetopause to the position of MMS $R_{MMS} =$
 400 (X, Y, Z) .

401 Throughout the text, when referring to subsolar jets an extra criterion is applied:

$$\begin{aligned} |Y_{GSE}| &< 2R_E \\ |Z_{GSE}| &< 2R_E \end{aligned} \quad (10)$$

402 where $|Y_{GSE}|$ and $|Z_{GSE}|$ are the absolute value of the y and z coordinate of the MMS
 403 satellite at the time of maximum dynamic pressure of each jet. Applying this criterion
 404 generated a smaller subset of jets ($n = 298$). This set is used to investigate relations
 405 between distances from the bow shock. We do so because a jet close to a subsolar po-
 406 sition with a dominant x velocity component is more likely to have travelled a distance
 407 approximately equal to the x distance between MMS and the bow shock.

408 To investigate the orientation of the flow, we calculate two more quantities. First,
 409 we calculate the velocity in the yz plane (V_ρ), and then the angle between that veloc-
 410 ity and the x axis. The velocity V_ρ is defined as:

$$V_\rho = \sqrt{V_y^2 + V_z^2} \quad (11)$$

411 while the angle is defined as:

$$\theta_{V_\rho} = \arctan\left(\frac{V_\rho}{|V_x|}\right). \quad (12)$$

412 An interesting quantity we investigated is the angle between the magnetic field vec-
 413 tor before and after the jet. This was done in order to search for any interesting prop-
 414 erties that could link a jet class to the pressure pulses connected to rotational discon-
 415 tinuities that were first described by Archer et al. (2012). To calculate the magnetic field
 416 angle we took the average of the magnetic field vector for 30 sec, 1 min and 2 min be-
 417 fore and after the jet and determined the angle between the "averaged" magnetic field
 418 measurements. All the derived quantities provided similar average and median results,
 419 although the actual values varied slightly. We have decided to use the 30 sec averaged
 420 magnetic field for the computation of the presented magnetic field angle.

$$\theta_B = \arccos\left(\frac{\langle \mathbf{B} \rangle_{\Delta t_1} \cdot \langle \mathbf{B} \rangle_{\Delta t_2}}{|\langle \mathbf{B} \rangle_{\Delta t_1}| |\langle \mathbf{B} \rangle_{\Delta t_2}|}\right) \quad (13)$$

421 where Δt_1 is a 30 sec duration before the jet and Δt_2 a 30 sec duration after the jet.

422 Another quantity that is considered is the angle between the average velocity vec-
 423 tor of the jet and the velocity vector of the surrounding plasma. This is computed by
 424 taking the average vector of the jet period and finding its angle to the average velocity
 425 vector taken 5 minutes before and after the jet. In order to have a velocity that better
 426 characterized the background flow of the plasma, we removed 30 seconds before and af-
 427 ter the jet when computing the average background velocity vector.

$$\theta_V = \arccos\left(\frac{\langle \mathbf{V} \rangle_{\Delta t_{jet}} \cdot \langle \mathbf{V} \rangle_{\Delta t_2}}{|\langle \mathbf{V} \rangle_{\Delta t_{jet}}| |\langle \mathbf{V} \rangle_{\Delta t_2}|}\right) \quad (14)$$

428 where, Δt_{jet} is the jet period and Δt_2 is an 9-minute duration, of 4.5 minutes before $t_{1,start} -$
 429 $30s$ and after $t_{1,end} + 30s$.

430 To investigate the total effect of each jet we calculated the integrated dynamic pres-
 431 sure over the jet's duration along the flow (total fluence) as:

$$f_{total} = \int P_{dyn} \cdot |\mathbf{V}| \cdot dt = \sum_i^n P_{dyn,i} \cdot |\mathbf{V}_i| \cdot \Delta t \quad (15)$$

432 where, n is the number of measurements within each jet period and Δt is the time res-
 433 olution of the FPI instrument (4.5 seconds).

434 We also present correlation coefficients between a number of jet properties. The
 435 most commonly used correlation coefficients are the Pearson's correlation coefficient (PCC)
 436 and Spearman's rank correlation coefficient (ρ_{Sp}). The former describes a possible lin-
 437 ear relationship between the two variables while the second is showing the strength of
 438 a monotonic relation (Myers et al., 2013). For our analysis, we use the Spearman's co-
 439 efficient to determine correlations between jets' quantities.

440 Throughout the results section, all plots are color-coded the same way. Qpar jets
 441 are represented by blue, Qperp by red, boundary by black and encapsulated by orange.

4 Results

The first observation, as shown in Table 3, is that the number of jets found downstream of the quasi-parallel shock is significantly higher than the number found in other classes. Boundary and quasi-perpendicular jets are less frequent and finally, encapsulated jets occur very rarely. While we cannot derive how frequently each jet occurs for each magnetosheath region (Qpar and Qperp), one can assume that on average the magnetosheath region during MMS orbits is equally distributed between the two regions (S. Petrinec, 2013). With that assumption, we can estimate that quasi-parallel jets occur much more frequently than quasi-perpendicular jets. Specifically, they can occur $\sim 5 - 10$ more often, depending on how many of the uncertain jets could be classified as Qpar jets (41.2% of the detected jets are unclassified, see Table 3). This result is in agreement with recent results showing that the frequency of Qpar jets can be ~ 9 higher than Qperp jets (Vuorinen et al., 2019).

4.1 Properties of the Jet Classes

In Figures 4 - 10, the basic properties of each class along with the quantities defined in the previous section are shown.

Starting with the basic properties of the jets in Figure 4, quasi-parallel and boundary jets have on average much higher dynamic pressure ($\langle P_{max} \rangle \sim 3$ nPa) compared to the quasi-perpendicular jets (~ 0.5 nPa), while encapsulated jets lie somewhere in between. Similar contrast between classes can be observed for the differences in dynamic pressure from the background magnetosheath plasma with or without solar wind normalization. The distributions and the average values of the absolute ion velocity show that the velocities of Qperp jets are much lower than these of Qpar, boundary and encapsulated jets. Interestingly, while this effect holds regardless of the normalization technique, when normalizing to the solar wind, the difference in velocity between classes is reduced. This could mean that on average the velocity of a jet primarily depends on the solar wind velocity at the time of its formation. Furthermore, it shows that the majority of Qperp jets are found under low solar wind velocities. Regarding the ion density, Qpar and boundary jets have on average twice as high density as the Qperp and encapsulated jets. When looking at the difference values however, the actual density gain is an order of magnitude more for the Qpar and boundary cases compared to the other two. Finally, the overall net gain of density and velocity for the jets is much higher for the rest of the classes compared to the Qperp jets.

In general, Figure 4 shows that the properties of Qpar and boundary jets are very similar, while both velocity and density changes in the Qperp jets are much smaller. This could imply differences in their generation mechanisms. Finally, encapsulated jets are dominated by an increase in velocity with absolute velocities gain being even higher than Qpar jets while their density distribution is very similar to Qperp jets.

For all jet classes, there are several jets where the dynamic pressure reaches values even higher than the dynamic pressure of the solar wind as expected from earlier studies (Plaschke et al., 2013). Only one encapsulated jet was found to have a higher velocity than its associated average solar wind velocity, while all other jets had a lower one. We can conclude that the main contribution of the dynamic pressure increase compared to the solar wind is due to the compression that solar wind undergoes after interacting with the bow shock. This, in turn, causes a density increase that can be several times higher in the jets compared to the solar wind.

The average and median jet duration of the main class jets is found to be 39 and 18 seconds respectively. As shown in Figure 5, Qpar and encapsulated jets have a slightly longer duration than boundary jets, while the Qperp jets have a much shorter duration, with the majority consisting of only 1 data point which corresponds to 4.5 seconds. To

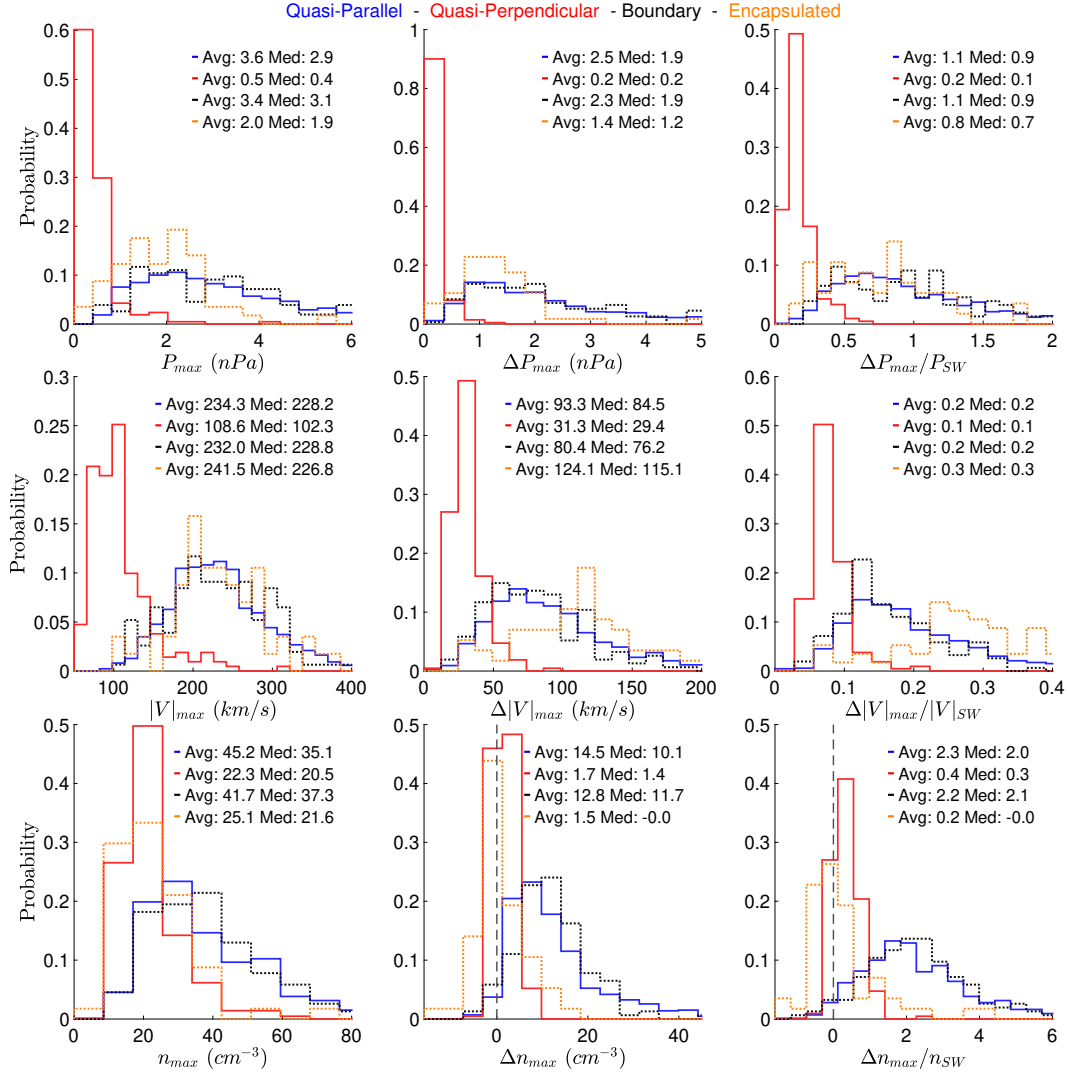


Figure 4. Histograms showing distributions, average and median values for the maximum values of the basic jet quantities. Maximum dynamic pressure, absolute velocity and density are shown. First columns show the measured values, the second describe the difference from the background and the third are normalized to the associated solar wind values.

492 investigate the low duration of Qperp jets, we explored the statistical properties of Qperp
 493 jets that contained at least 3 data points (69/211 cases). Doing so, we discovered that
 494 their basic properties (Figure 4.) are statistically similar to the whole subset and there-
 495 fore it was decided that all the jets can be included in the analysis. It should be noted
 496 that the duration of encapsulated jets is biased to appear longer by their definition (Ta-
 497 ble 2), since shorter jets would be classified as Qpar.

498 In Figure 5, when looking at the dynamic pressure integrated over the jet period
 499 (Eq. (15)) we see a consistent picture where the shorter duration along with the lower
 500 dynamic pressure make the Qperp jets much weaker in comparison to the rest of the jet
 501 classes. On average the rest of the jets seem to be similar while the Qpar and bound-
 502 ary jets, again hold very similar properties. The distance from the bow shock (Eq. (8))
 503 is quite different for each class. While boundary and Qpar have similar relative positions,
 504 the Qperp jets are found further inside the magnetosheath. This difference is more vis-

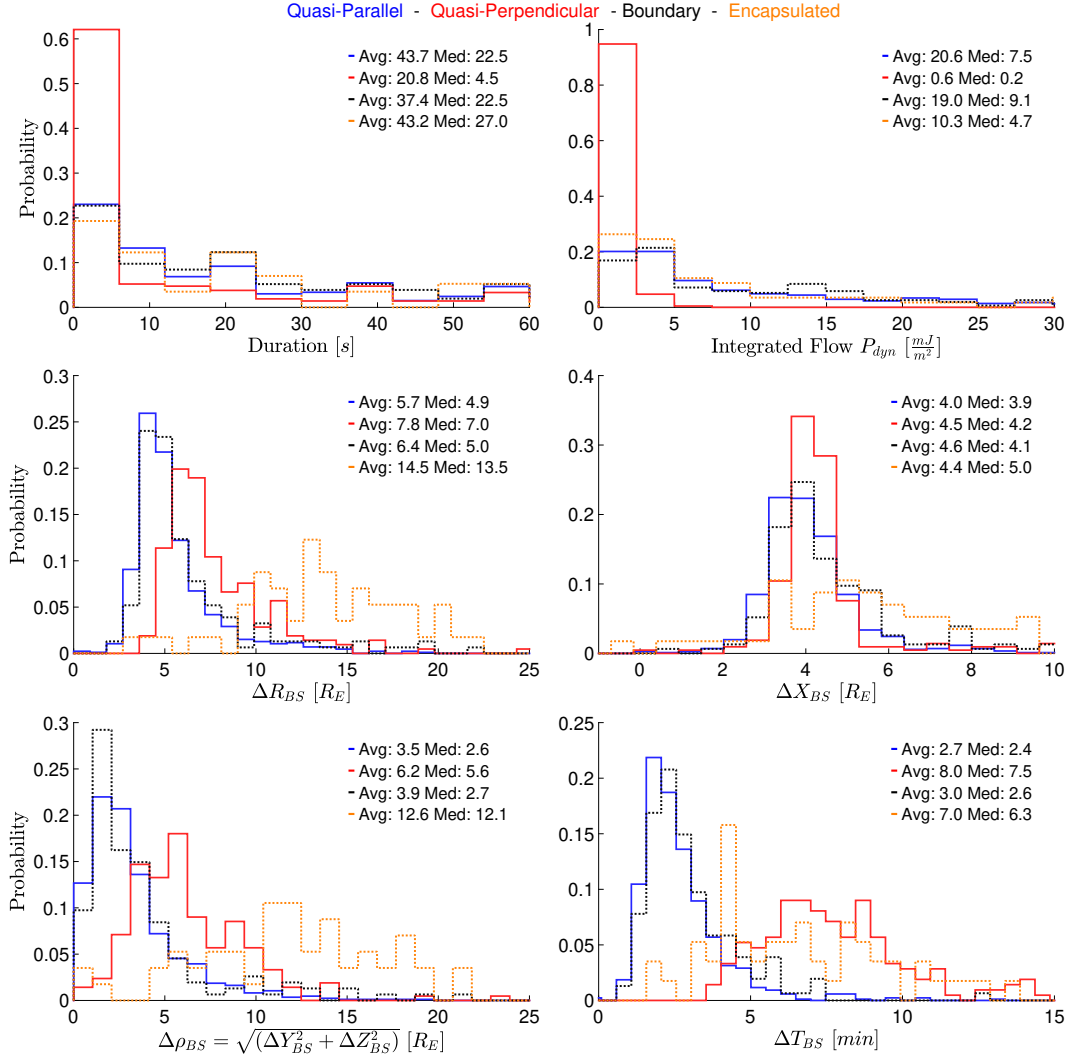


Figure 5. Histograms showing distributions, average and median values for scale sizes and for distances, estimated from a point of origin at the bow shock for each jet. ΔT_{BS} describes the time that was estimated for the jet to arrive to MMS from its origin point at the bow shock.

505 ible when looking at the distance on the yz plane from the bow shock. Encapsulated jets
 506 are also found at a much higher radial distance (R) from the bow shock, again with the
 507 ρ component having much higher values than the rest of the classes. It should be noted
 508 that Qperp jets are found to occur primarily under low-velocity solar wind conditions.
 509 As a result, the bow shock model used for those cases generates a bow shock further away
 510 from the Earth than for the cases of Qpar and Boundary jets. Finally, the time that it
 511 took each jet to reach the MMS is much different. Qpar and boundary jets need on aver-
 512 age ~ 3 minutes while the much slower Qperp jets require much more at around \sim
 513 8 minutes. Encapsulated jets also take a long time to reach MMS from their origin point
 514 (~ 7 min) but in contrast to Qperp jets, this is due to the large distance that they have
 515 to cover rather than their velocity.

516 To analyze the different geometric properties of each class, we also include Figure.
 517 6, showing the distance of the jet from the Earth and the distance from a magnetopause
 518 model (Eq. 9). It is shown that while jets of every class are found in similar distances

519 from the Earth (position of MMS), the distance from the magnetopause varies consid-
520 erably. While Qperp jets are expected to appear closer to the magnetopause from their
521 corresponding distance of the bow shock (Figure 5), it is now clear that they occur so
522 close to the magnetopause that often they appear to be within the magnetosphere due
523 to the inaccuracies of the model in use. It should be stressed that encapsulated jets are
524 not only found close to the magnetopause but they are also found closer to the Earth
525 (Figure 6, right).

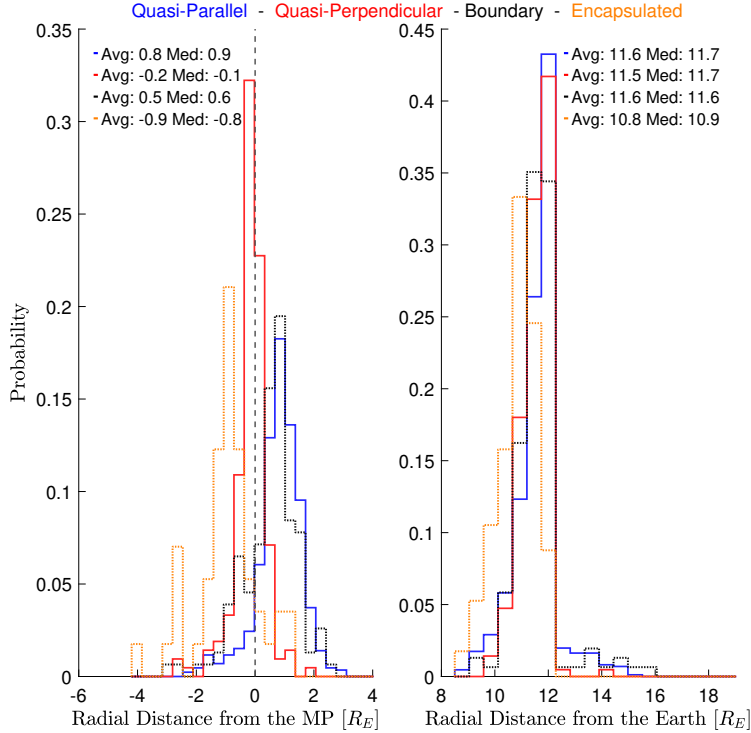


Figure 6. Histograms showing distributions, average and median values of the jets’ distance from the magnetopause and from the Earth

526 Figure 7 shows that the ion temperature profiles are quite different between each
527 class. On average, the temperature is lower on Qperp jets (~ 100 eV) compared to the
528 rest of the jets (~ 300 eV). The difference of both T_{\perp} and T_{\parallel} compared to the background
529 is negative and very similar between boundary and Qpar jets. On the other hand, it is
530 around zero for Qperp jets and positive for the encapsulated jets. Most of the observed
531 differences are expected due to the nature of the magnetosheath region and from the def-
532 inition of each class. As mentioned in the previous subsection, encapsulated and bound-
533 ary jets have a very different background magnetosheath. Therefore, a direct compar-
534 ison between each class can be misleading, especially in the case of the highly variant
535 temperature measurements.

536 An interesting difference regarding the mean absolute magnetic field appears in Fig-
537 ure 7. Qpar jets have on average, a smaller mean absolute magnetic field than the rest
538 of the classes ($\langle |B|_{mean} \rangle \sim 25$ nT). Encapsulated jets have almost twice as high val-
539 ues while the mean absolute magnetic field of Qperp and boundary jets’ is in between,
540 at $\langle |B|_{mean} \rangle \sim 30$ nT.

541 The difference in the mean absolute magnetic field ($\Delta |B|_{mean}$) is higher in Qpar
542 and boundary jets compared to Qperp and encapsulated jets. Specifically, Qpar and bound-

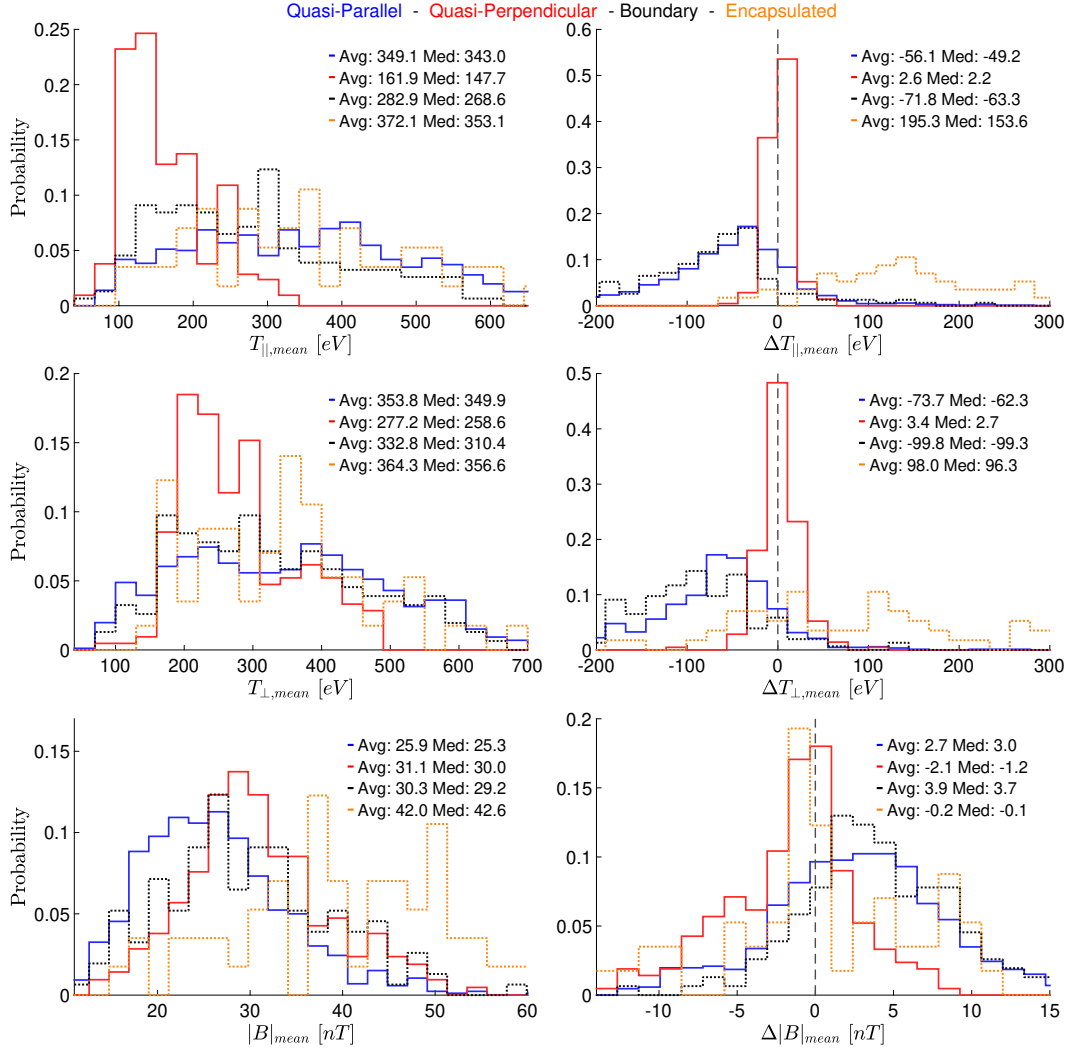


Figure 7. Histograms showing distributions, average and median values for the average values of ion temperature and absolute magnetic field.

543 any jets have a bigger absolute magnetic field than their background magnetosheath. On
 544 the other hand, Qperp jets have on average a slightly smaller magnetic field although
 545 the actual values range for individual events vary significantly ($\Delta|B|_{mean} \in [-10, 10]$
 546 nT).

547 Figure 8 shows how plasma (thermal) and magnetic pressures vary between each
 548 class along with their ratio (β parameter). For all the classes, the maximum plasma pres-
 549 sure is on average higher than the maximum magnetic pressure. However, when look-
 550 ing at the difference values, the Qpar, and the boundary jets have higher maximum mag-
 551 netic pressure ($\Delta P_{magnetic,max}$) than maximum plasma pressure ($\Delta P_{plasma,max}$). On the
 552 other hand, Qperp and encapsulated jets still have a higher maximum thermal pressure
 553 difference than maximum magnetic pressure difference. Looking at the maximum mag-
 554 netic pressure and its difference to the background can also be directly interpreted as
 555 a measurement of the maximum absolute magnetic field. This information shows us that
 556 although from the previous histograms (Figure 7), the average magnetic field ($|B|_{mean}$)
 557 is higher in the case of Qperp jets, the maximum ($|B|_{max}$) values are higher in the Qpar
 558 and boundary cases. This could originate from the higher duration of Qpar jets, along

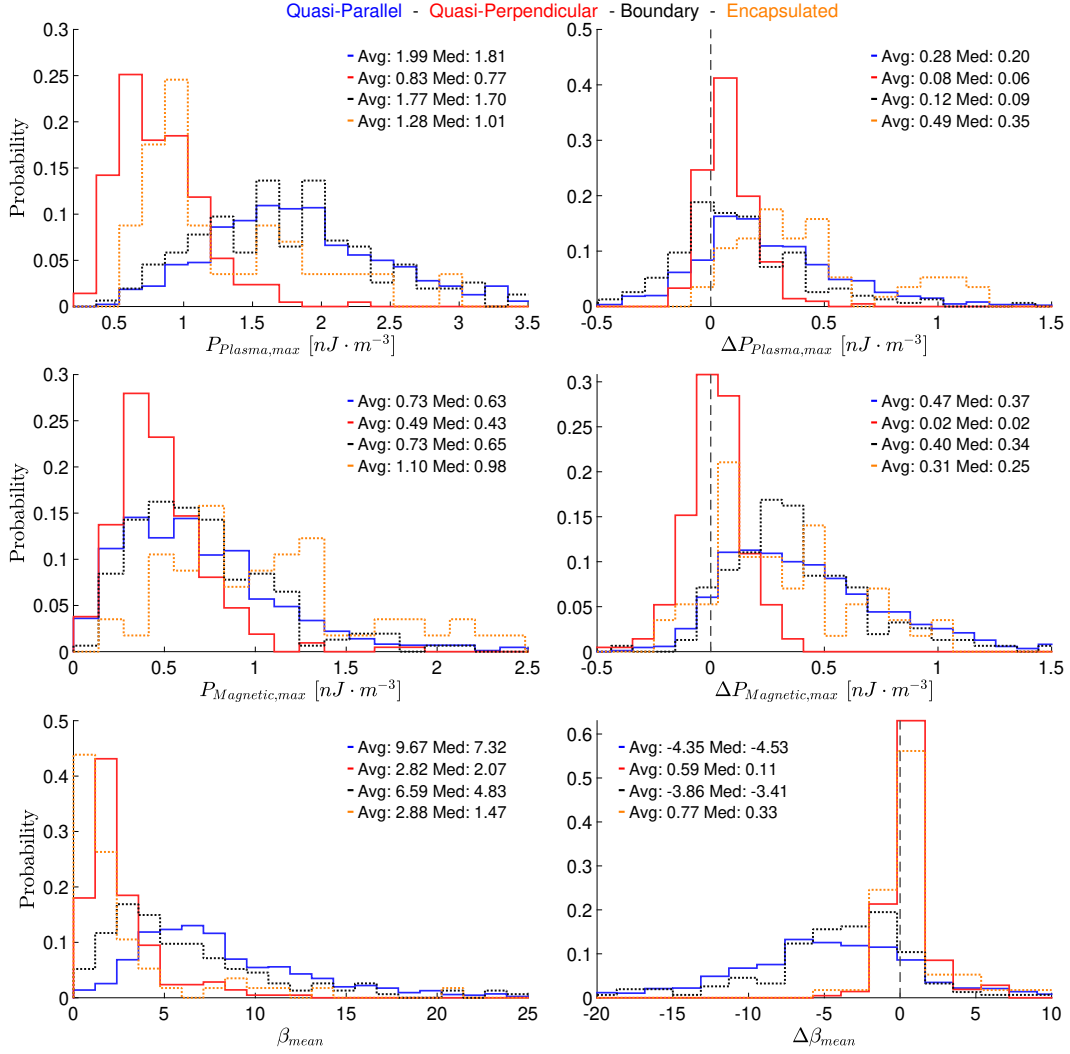


Figure 8. Histograms showing distributions, average and median values for the maximum plasma pressure, the maximum magnetic pressure and the mean β parameter.

559 with the higher time resolution of the FGM data compared to the FPI. These two fac-
 560 tors can allow very high magnetic field values to occur within a jet period since in prin-
 561 ciple $|B|$ can have a higher variance in the quasi-parallel environment. The behavior of
 562 the β parameter is consistent with the previous results. While it is higher for the Qpar
 563 and boundary classes, it is on average smaller than that of the background plasma around
 564 the jets. On the other hand, encapsulated and Qperp jets have on average smaller beta
 565 values but still maintain a positive difference when compared to the background.

566 Specifically, average beta values appear to be closer to unity for the Qperp and en-
 567 capsulated cases, while they are on average higher ($\langle \beta_{qpar} \rangle \sim 10$, $\langle \beta_{boundary} \rangle \sim 6$)
 568 for the other classes. When looking at the difference to the background, it appears that
 569 Qpar and boundary jets have a negative beta difference ($\Delta \beta < 0$). This could indicate
 570 that magnetic pressure has a larger effect in the jet than in the surrounding magnetosheath
 571 plasma.

572 The velocity components of each class are shown in Figure 9. Here, we present the
 573 absolute velocity for the y and z component. This was done because all jets and espe-

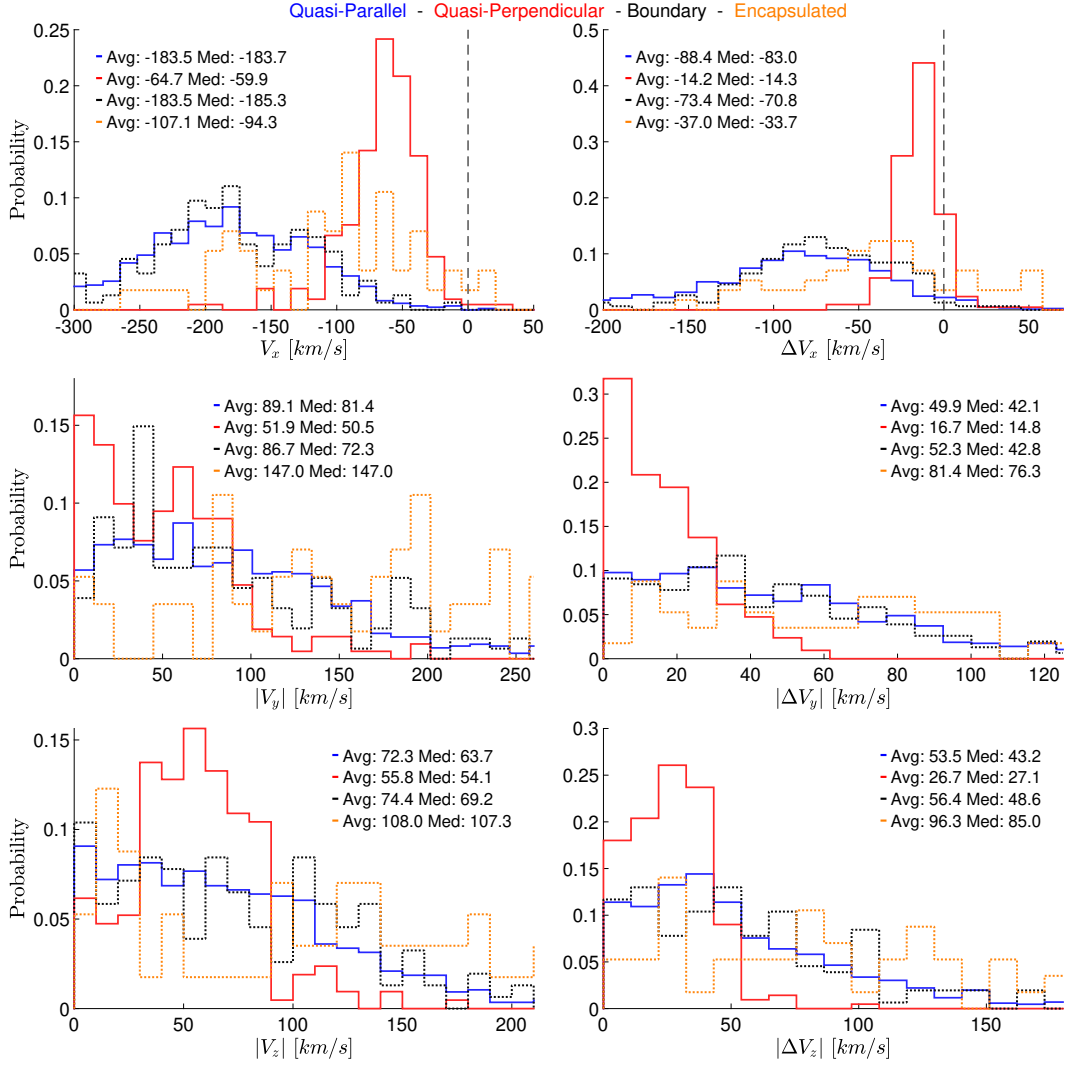


Figure 9. Histograms showing distributions, average and median values for each velocity component at $|V|_{max}$.

574 cially encapsulated jets had a distribution that produced an average velocity close to zero,
 575 in both components, due to equally frequent jets exhibiting a high negative and posi-
 576 tive $V_{y,z}$. As a result, providing a histogram without the absolute values would limit the
 577 information of each class, and would not contribute to a meaningful comparison.

578 As expected, almost every jet has a dominating negative (earthward) x component,
 579 with the Qperp jets on average having smaller values on every velocity component com-
 580 pared to the other classes. Furthermore, Qperp jets seem to have very similar velocities
 581 in all three components which are different from the rest of the classes that tend to have
 582 a more significant imbalance between components. An interesting difference can be seen
 583 in the encapsulated jets where the dominant component of their velocity is surprisingly
 584 V_y and V_z . The same effect can be seen when we look at the absolute difference ($|V_{jet} -$
 585 $V_{MSH}|$), where the difference to the background seems to be higher for the Qpar and bound-
 586 ary jets than Qperp jets, while encapsulated exhibit values much higher than the rest
 587 of the classes.

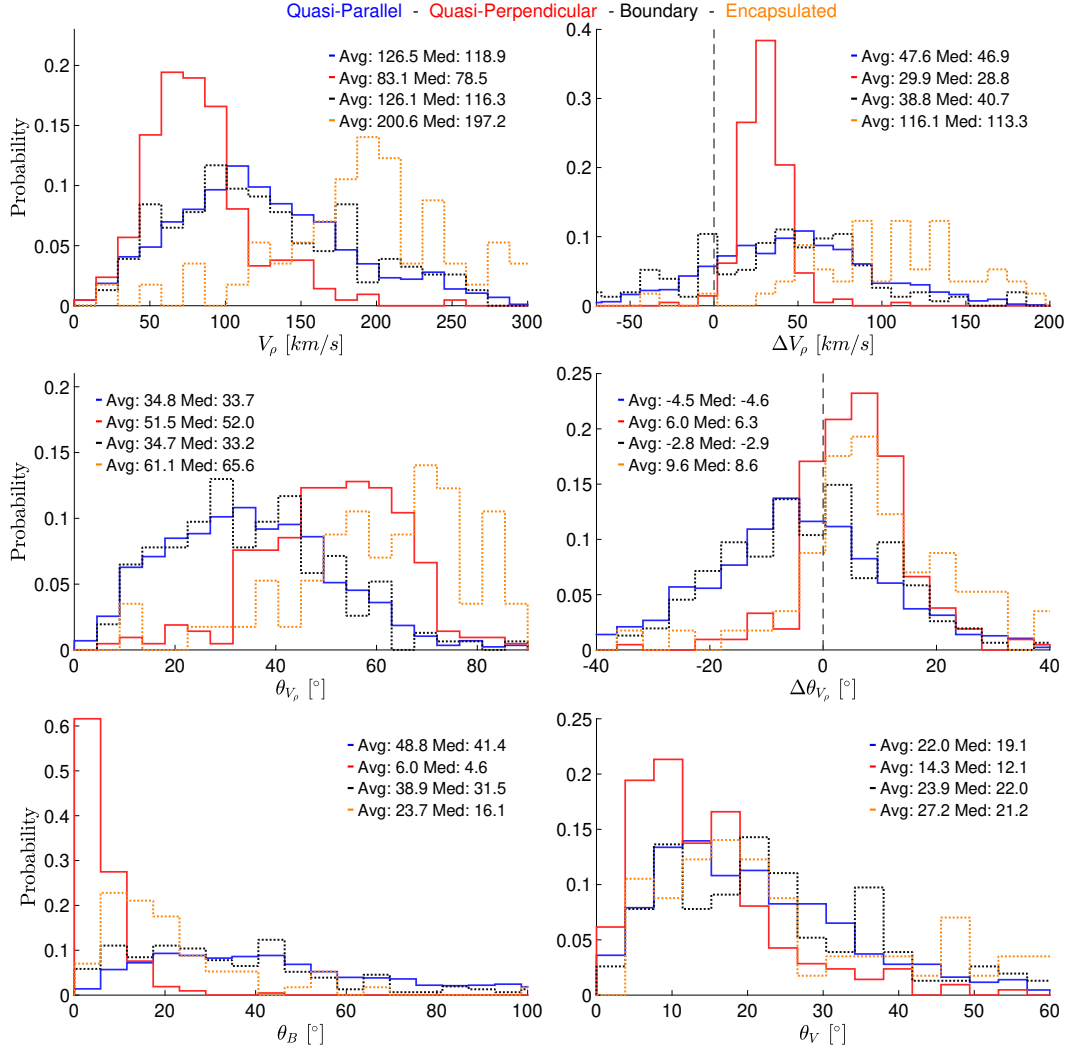


Figure 10. Histograms showing average and median values for directional information and changes in the magnetic field and velocity vectors. In particular, the angle between the x velocity component and the yz plane is investigated (θ_{V_ρ}). Furthermore, two angles showing the difference in the magnetic field vector (θ_B) and the velocity vector (θ_V) between the periods before and after the jet periods are also shown.

588 Finally, in Figure 10, directional information and rotation angles of the magnetic
 589 field and the velocity are given. As expected, the yz plane velocity (V_ρ) is much higher
 590 for the encapsulated jets compared to the other three classes. This can also be seen
 591 when calculating the angle between the jet's velocity and the x axis (Eq. (12)), in which the
 592 Qpar and boundary jets show similar behavior, while Qperp jets have on average a higher
 593 angle and encapsulated jets the highest. This picture is consistent when comparing to
 594 the background plasma in which Qpar and boundary jets show a net decrease in the
 595 angle while Qperp and encapsulated show a net increase. Looking at the magnetic field
 596 rotation angle (Eq. (13)), there seems to be a significant difference between the Qperp jets
 597 and the other classes. Qperp have on average a very small ($\sim 6^\circ$) difference while the
 598 rest of the classes have on average higher values, particularly the Qpar jets. Consider-
 599 ing velocity rotation angles (Eq. (14)), Qperp jets exhibit the least changes, although
 600 all classes seem to have similar statistical values and distributions.

601 It should be noted that since both velocity and magnetic field rotation angles de-
 602 scribe the changes between the plasma before and after jet, the results are heavily af-
 603 fected by the duration of the jet. Specifically, it is expected that jets with a shorter du-
 604 ration such as Qperp jets would statistically have a smaller angle change since measure-
 605 ments taken are spatially and temporally closer to each other.

606 4.2 Relation Between Jet Properties

607 In this subsection, we will report on some observations on correlations between dif-
 608 ferent jet properties. It should be noted that all correlations mentioned were found to
 609 have a p-value of less than 0.01, unless stated otherwise. The computation of the p-value
 610 was done through the exact permutation distributions of each subset (Edgington, 2011).

611 There is a moderate correlation between the magnetic field rotation angle (θ_B) and
 612 both the maximum dynamic pressure (P_{max}) and the difference of maximum dynamic
 613 pressure compared to the background (ΔP_{max}).

614 Specifically, regardless of the way we calculated the magnetic field rotation angle,
 615 for all jets found in the main classes, we found a moderate correlation using Spearman's
 616 coefficient, $\rho_{Sp,All} = 0.43 \pm 0.02$. Considering only subsolar jets this correlation was
 617 increased, reaching $\rho_{Sp,Subsolar} = 0.6 \pm 0.05$.

618 A possible interpretation could be that the jets distort the magnetic field lines that
 619 are embedded in the plasma in front of them. On weaker jets such as in the majority of
 620 Qperp jets (Figures 4 and 10) this effect would be hardly visible since we see the dynamic
 621 pressure being an order of magnitude less compared to the other classes and the mag-
 622 netic field rotation angle is also close to zero. On the other hand, on jets that on aver-
 623 age have a higher velocity and density gain, magnetic field vector seems to be different
 624 in the plasma in front and behind the jet. To investigate this possible link, we look at
 625 class-specific correlation coefficients. For the classes of Qperp and Qpar jets, it was found
 626 that the correlation is almost non-existent ($\rho_{Sp,\perp,\parallel} = 0.1 \pm 0.05$ (p-value = 0.04)). As
 627 a result, we conclude that the correlation was caused by the different properties of each
 628 class causing an artificial correlation that does not necessarily represent a physical prop-
 629 erty. The above result emphasizes the importance of classifying jets that physically oc-
 630 cur in different environments before drawing any strong conclusions.

631 In Figure 11, a comparison between the density and the velocity squared difference
 632 normalized by the total dynamic pressure gain is shown, similar to Figure 3 of Archer
 633 and Horbury (2013). Figure 11(a) shows the relative change in density and velocity with
 634 measurements taken at the point of maximum dynamic pressure. In Figure 11(b) how-
 635 ever, the difference is taken by using the measurements of maximum density, velocity
 636 and dynamic pressure for each quantity. As shown in Figure 11, the majority of the jets
 637 have a combination of velocity and density increase, contributing to the overall dynamic
 638 pressure enhancement. For the Qpar and boundary cases, less than 0.5% jets are purely
 639 velocity driven, exhibiting a density decrease compared to the background plasma. On
 640 the other hand, Qperp jets can have a decrease in density up to 22% and encapsulated
 641 jets up to 68% of the times, making their dynamic pressure to mainly originate from a
 642 velocity increase. More information regarding the velocity and density distribution of
 643 each class can be found in Table 4. As expected, most of the jets regardless of their class
 644 exhibit an increase in both density and velocity when comparing to the background mag-
 645 netosheath. This result shows that the increased frequency of Qpar and boundary jets
 646 can be at least partially attributed to density enhancements taking place, while being
 647 insignificant or even absent in the case of Qperp jets. It should be noted that the val-
 648 ues in parentheses shown in Table 4 correspond to the same time (P_{max}) and are there-
 649 fore a better metric for quantifying the cases that exhibit a density decrease. However,
 650 the calculation that includes the maximum density and velocity points are also impor-
 651 tant as they are measured within the jet period as seen by MMS. These values act as

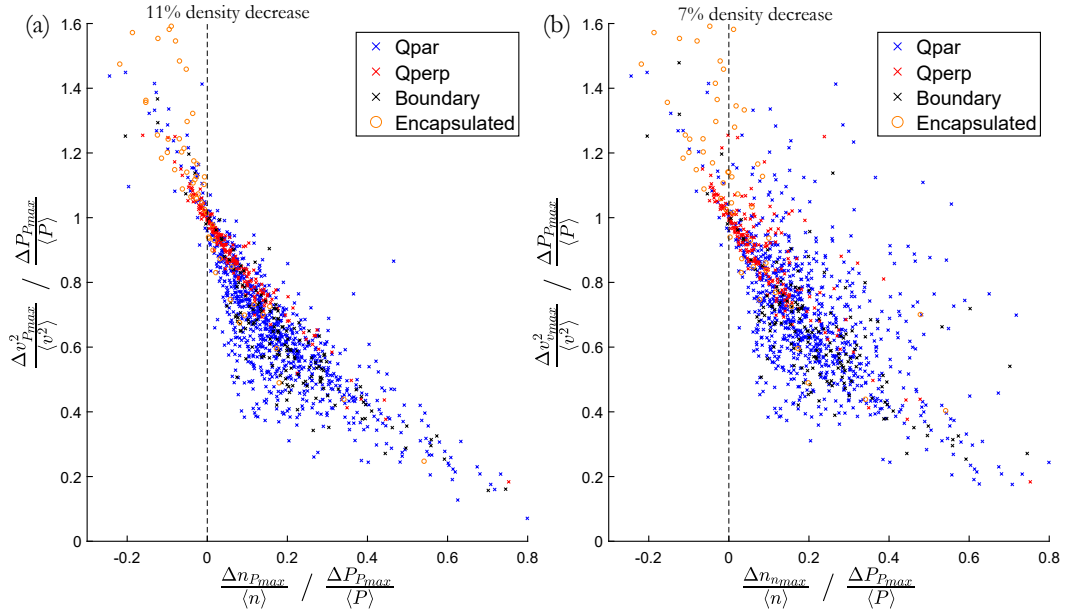


Figure 11. (a): Relative difference in density and velocity at the time of maximum P_{dyn} . (b): Relative difference in density and velocity for the maximum value of each quantity, measured within the jet period.

652 the lowest limit case metric, showing how many jets exhibit an increase or decrease in
 653 velocity and density.

654 When comparing our results to earlier studies, we find that they are quite similar.
 655 In particular, depending on the normalization technique 7 – 11% of the jets exhibit a
 656 relative decrease in density with the increase in dynamic pressure being caused by a very
 657 high enhancement of absolute velocity. Plaschke et al. (2013) found 10.5% using a dif-
 658 ferent jet criterion, while Archer et al. (2012) using essentially the same criterion as this
 659 work found 18%. In the main classes, we find no cases exhibiting a velocity decrease as
 660 shown in Figure 11 and Table 4. In order to see if there are any jets showing a veloc-
 661 ity decrease, we searched the full jet database ($N = 8499$). The only cases with a ve-
 662 locity decrease were 158 jets from which 151 have been classified as ”Border” jets, found
 663 too close to either the magnetopause or the bow shock. Therefore, since any calculation
 664 averaging over different plasma regions is statistically unreliable, we exclude them. Care-
 665 ful examination on the rest of the 7 cases showed that they were jets that occurred very
 666 close to another jet but not close enough to fulfill the criteria of jet combining (Eq. (3)).
 667 As a result, we conclude that there are no jets showing a relative velocity decrease at their
 668 maximum dynamic pressure measurement.

669 In Figure 12 we present two different types of cross-plots. In subplots (a) and (c),
 670 plots of the difference in maximum density (Δn_{max}) against difference in maximum mag-
 671 netic field ($\Delta |B|_{max}$) with and without solar wind normalization are shown. This was
 672 done in order to test a hypothesis that connects SLAMS to the generation of Qpar jets
 673 (Archer et al., 2012; Karlsson et al., 2015) We, therefore, search for some kind of cor-
 674 relation between the density increase and the magnetic field increase since SLAMS have
 675 such a correlation (Schwartz & Burgess, 1991; Behlke et al., 2003). In the sub-figures (b)
 676 and (d) we similarly investigate the difference of maximum velocity (ΔV_{max}) against the
 677 difference in minimum ion temperature (ΔT_{min}). This was done to see if a correlation
 678 can be found that could support the mechanism proposed by Hietala et al. (2009) that
 679 associates jets with ripples of the quasi-parallel bow shock. As discussed and shown in

Table 4. Velocity and density distribution of jets that exhibit a dynamic pressure increase. First values are based on the maximum quantity met within jet’s duration and values in parenthesis are derived from the density and velocity value found at P_{max} .

Class	Velocity Decrease (%)	Density Decrease (%)
	$V_{max}(V_{P_{max}})$	$n_{max}(n_{P_{max}})$
All	1.6 (1.8)	6.9(10.9)
Main Classes	0 (0)	7.3(10.8)
Quasi - Parallel	0 (0)	2.9(5.23)
Quasi - Perpendicular	0 (0)	15.6(22.3)
Boundary	0 (0)	3.9(5.2)
Encapsulated	0 (0)	50.1(68.4)

680 earlier studies, it is expected that the background plasma surrounding the ripple-generated
 681 jet would be more decelerated and would, in turn, have a higher temperature compared
 682 to the jet flow created by passing through a ripple of the bow shock, undergoing less de-
 683 celeration, and heating (Hietala & Plaschke, 2013; Plaschke et al., 2013).

684 As shown in Figure 12(a,c), for the quasi-perpendicular jets, there is no significant
 685 correlation between the difference in maximum magnetic field (ΔB_{max}) and the differ-
 686 ence in maximum density (Δn_{max}). However, in the case of quasi-parallel jets, there is
 687 a moderate monotonic relationship between the two quantities. Spearman’s rho value
 688 (ρ_{Sp}) for the quasi parallel case is $\rho_{Sp,a,\parallel} = 0.57$ and $\rho_{Sp,c,\parallel} = 0.55$, whereas for the
 689 quasi-perpendicular jets is $\rho_{Sp,a,\perp} = -0.2$ and $\rho_{Sp,c,\perp} = -0.27$. For all the jets to-
 690 gether, a total correlation of $\rho_{Sp,a} = 0.66$ and $\rho_{Sp,c} = 0.63$ is reached. Indices a, b, c, d
 691 refer to the subplots of Figure 12, while the symbols of parallel and perpendicular refer
 692 to Qpar and Qperp jets respectively.

693 These results support the idea that a subset of quasi-parallel jets may originate from
 694 a SLAMS interacting with bow-shock ripples as described by Karlsson et al. (2015). Fur-
 695 ther support of this mechanism is shown when looking back at the general characteris-
 696 tics of each class. In Figure 4 it is shown that Δn_{max} is an order of magnitude higher
 697 for the Qpar jets compared to the Qperp. Furthermore, in Figure 7, Qpar jets exhibit
 698 on average a positive difference on the average absolute magnetic field compared to the
 699 Qperp jets that do not. Maximum magnetic pressure and average β values shown in Fig-
 700 ure 8 also support SLAMS since Qpar and boundary jets have not only a higher mag-
 701 netic pressure than Qperp jets, but also a higher value than their surrounding plasma.
 702 It should be noted, however, that the anti-correlation observed for Qperp jets can not
 703 be directly explained through any known mechanism. The observed anti-correlation should
 704 be treated with caution since it was only found for the "final cases" of Qperp jets (Ta-
 705 ble 3). When we look at the whole body of Qperp jets the observed correlation disap-
 706 pears.

707 In Figure 12(b,d) a weak/moderate linear correlation between the difference in min-
 708 imum temperature (ΔT_{min}) and the difference in maximum absolute ion velocity (ΔV_{max})
 709 is shown. Correlation coefficients are found to be $\rho_{Sp,b} = -0.35$ and $\rho_{Sp,d} = -0.5$ when
 710 looking at the whole body of the jets. While looking exclusively at Qpar jets, we find
 711 $\rho_{Sp,b,\parallel} = -0.28$ and $\rho_{Sp,d,\parallel} = -0.43$. On the other hand, when looking at Qperp jets,
 712 we find correlation coefficients of $\rho_{Sp,b,\perp} = -0.24$ and $\rho_{Sp,d,\perp} = -0.23$.

713 All main class jets have a small to medium anti-correlation relation between the
 714 ion temperature and the velocity difference within the jet period (Figure 12(b,d)). As
 715 discussed previously, we can interpret this result as indirect support of a mechanism that

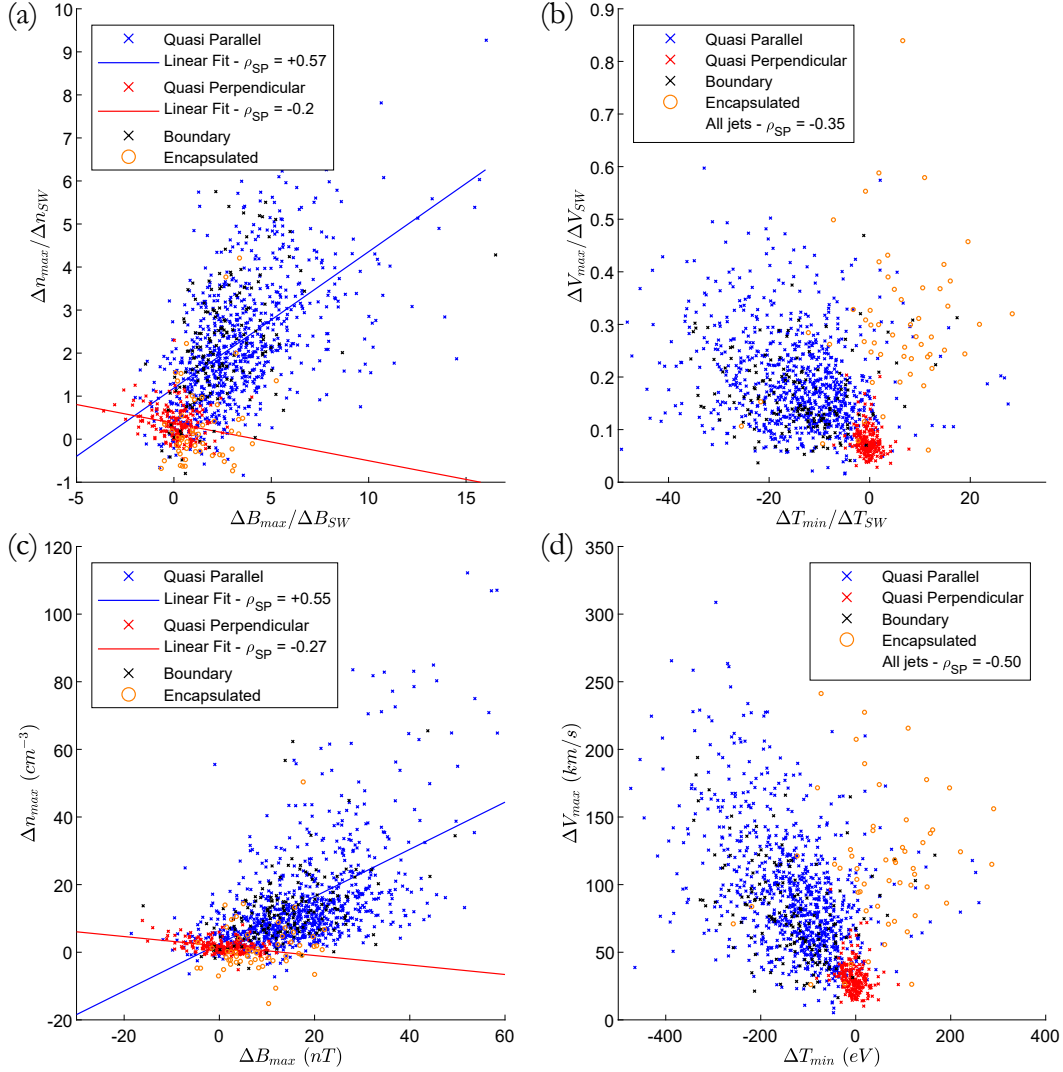


Figure 12. (a): Δn_{max} against $\Delta|B|_{max}$ normalized over solar wind data. Linear regression lines are shown for visual guidance, for the Qpar (blue) and Qperp (red) cases. (b): ΔV_{max} against ΔT_{min} normalized over solar wind data. (c): Δn_{max} against $\Delta|B|_{max}$. Linear regression lines are shown for visual guidance, for the Qpar (blue) and Qperp (red) cases. (d): ΔV_{max} against ΔT_{min} . In all figures every point represents a jet while the color shows its class.

716 is based on the bow shock ripple idea (Hietala et al., 2009; Hietala & Plaschke, 2013).
 717 This result is also supported by the general properties shown in Figure 7, where for Qpar
 718 jets there is a larger difference between the temperature of the background magnetosheath
 719 plasma and the jet. Finally, it has been recently found that similar ripples can be found
 720 also at the quasi-perpendicular bow shock which could mean that the generation mech-
 721 anism of these jets is of the same nature (Johlander et al., 2016). Although the major-
 722 ity of the jets seem to have a medium anti-correlation that could support Hietala's mech-
 723 anism (Hietala et al., 2009; Hietala & Plaschke, 2013), we cannot say the same for the
 724 quasi-perpendicular where the anti-correlation is weaker. It should be noted, however,
 725 that due to the very small duration of the jets, there is usually only one measurement
 726 for the temperature and the velocity. Therefore, there is a higher uncertainty regard-
 727 ing this result compared to the other classes.

728 Finally, based on the differences between thermal and magnetic pressure shown in
729 Figure 8, we investigate possible relationships with other jet properties.

730 Regarding the difference in maximum magnetic pressure, there is a moderate to
731 strong correlation with the total integrated dynamic pressure $\rho_{Sp,All} = 0.72$. This re-
732 sult could be interpreted in terms of SLAMS similarly to the analysis of Figure 12 since
733 to calculate the total dynamic pressure we include the ion density (n). However, it was
734 found that all the factors of Eq. (15) are correlated to the maximum magnetic pressure
735 ($P_{mag,max}$), including the difference in maximum absolute velocity (ΔV_{max}) which had
736 a correlation coefficient of $\rho_{Sp,All} = 0.59$ and the duration which had a correlation of
737 $\rho_{Sp,All} = 0.62$. This result is unexpected and can be considered an indication that mag-
738 netic forces play a more important role than previously thought. Qpar jets have simi-
739 lar correlations, while Qperp jets are also alike, apart from the same anti-correlation shown
740 in Figure 12, regarding the density difference and $\Delta|B|$. It should be noted that this ef-
741 fect appears on all the jets and not only in the Boundary jets as initially speculated.

742 However, when looking at each class exclusively, the results show that the effect
743 decreases significantly for the duration and velocity for both Qpar and Qperp jets $\rho_{Sp} \sim$
744 0.2. The correlation (when taking all classes together) seems to have been artificially cre-
745 ated because in jets with higher velocities and duration it is relatively easier to measure
746 the magnetic field in higher values. This is made possible by the fact that longer dura-
747 tion jets could in principle allow more measurements of the magnetic field to occur and
748 due to the variance of the FGM measurements, reach a higher peak. This, in turn, cre-
749 ates a non-physical correlation between the maximum magnetic field measurement found
750 within a jet and its duration. The only effect that seems to be robust and even enhanced
751 when taking average quantities is the correlation between the density difference ($\Delta n_{mean,max}$)
752 and the absolute magnetic field difference ($\Delta|B|_{mean,max}$). Specifically, Qpar jets have
753 a positive correlation in all four possible combinations of the absolute magnetic field and
754 ion density quantities. The four combinations result when taking the average and max-
755 imum density and test their correlation with the average and maximum absolute mag-
756 netic field. Looking at these pairs, it as found that Qpar maintain a positive correlation
757 coefficient, $\rho_{Sp,||} \in [0.3, 0.6]$. Similarly, the anti-correlation of the Qperp jets remains
758 in all cases, $\rho_{Sp,\perp} \in [-0.28, -0.65]$. Once more, we should point out that the correla-
759 tion found in the Qpar jets remains high even when looking at all the Qpar jets rather
760 than the 'final cases' (Table 3). On the other hand, the observed anti-correlation is con-
761 siderably smaller for the Qperp jets.

762 From this result, we conclude that the magnetic field seems to play an important
763 role in forming the density profile of each class, possibly explained through SLAMS mech-
764 anism. The correlation found on other jets' properties although less consistent, could still
765 indicate that magnetic fields could have a more important role regarding the velocity and
766 duration of each jet.

767 An interesting difference was also found when investigating the difference in both
768 the maximum and the average thermal plasma pressure difference ($\Delta P_{th,mean,max}$).

769 Qpar jets when investigated with the maximum differences in density and thermal
770 pressure have a moderate correlation $\rho_{Sp,||} = 0.36$. However, when we take average val-
771 ues for density or thermal pressure, this correlation disappears fully. On the other hand,
772 as discussed previously, density changes are heavily correlated with the magnetic pres-
773 sure of the Qpar jets. This result shows that the changes in temperature are more im-
774 portant than the changes in density in deriving the thermal pressure difference. On the
775 other hand, Qperp jets have a high correlation of density change and thermal pressure
776 $\rho_{Sp,\perp} = [0.5, 0.7]$. This indicates that the contribution of density change in thermal pres-
777 sure difference is more important than the temperature difference for the Qperp jets.

5 Discussion and Conclusion

We have investigated the properties of an extensive dataset of magnetosheath jets ($N = 8499$) using MMS and classified them in different categories based on local magnetosheath measurements. The characteristics of the different classes correspond to plasma originating from the different values of the angle (θ_{Bn}) between the IMF and the bow shock's normal vector. The general properties found were in agreement with earlier studies. In particular, our dataset contains jets with an average duration of ~ 30 seconds, similar to what has been reported in other studies (Němeček et al., 1998; Savin et al., 2012; Archer & Horbury, 2013; Plaschke et al., 2013). Their dynamic pressure enhancement was found to be in most cases due to both velocity and density enhancement (Amata et al., 2011; Archer & Horbury, 2013; Plaschke et al., 2013; Karlsson et al., 2015). There was no clear case exhibiting a velocity decrease compared to the background magnetosheath, while for all the jets, velocity appears to always be smaller than the associated solar wind measurements. Finally, on average, most of the jets that can be appropriately normalized, have a lower temperature compared to their background. This is in principle expected for a flow that has been less heated and decelerated from the bow shock interaction as shown in previous studies (Savin et al., 2008; Amata et al., 2011; Hietala et al., 2012; Archer et al., 2012; Plaschke et al., 2013, 2018). We have additionally made a number of new observations that are discussed in the following subsections.

5.1 Quasi-Parallel and Quasi-Perpendicular Jets

The results of this study show that quasi-parallel jets are considerably more frequent than quasi-perpendicular jets. Specifically, similar to recent results (Vuorinen et al., 2019), they were found to occur ~ 5 – 10 times more frequently than quasi-perpendicular jets. On average they have a dynamic pressure around 3.5 nPa, with the majority of them exhibiting both a density and a velocity increase. Their density increase shows a significant correlation with the absolute magnetic field increase ($\rho_{Sp} = 0.5 \pm 0.2$) indicating a possible association of at least a subset of them to SLAMS. A moderate anti-correlation was found between the maximum velocity difference (ΔV_{max}) and the minimum temperature difference (ΔT_{min}). This could be interpreted as a relatively weak support of the bow shock ripple mechanism. Furthermore, the high magnetic field values and variance found could indicate possible wave activity that may contribute to their properties. Finally, most of the quasi-parallel jets are earthward with very high velocities, making them very interesting candidates to investigate phenomena such as jet-triggered magnetopause reconnection or other magnetosphere coupling phenomena.

Quasi-perpendicular jets have a much smaller dynamic pressure than the rest of the classes and their dynamic pressure is mainly due to a velocity increase rather than a density enhancement. Their duration is significantly smaller (median: 4.5 seconds per jet) and their total integrated dynamic pressure is more than an order of magnitude lower than the corresponding values of the other jet types. While their existence is clear according to the criterion used, their importance regarding magnetospheric influence is to be questioned.

Their properties, when compared to Qpar jets, suggest that either a different mechanism or a smaller scale version of Qpar generation mechanism causes their generation. The density differences can be in principle, attributed to the absence of SLAMS that are believed to occur only in the ion foreshock generated under quasi-parallel bow shock. On the other hand, we hypothesize that their low velocities compared to the other classes could be the result of one or more of the following effects. The jet criterion used (Eq. (1)) is fulfilled more easily during low dynamic pressure conditions compared to high dynamic pressure ones. As a result, there might be an observational bias causing MMS to observe primarily jets that occur under low-velocity solar wind conditions. Secondly, there might be a link between the actual solar wind conditions and the IMF orientation, in

829 which slower solar wind flow could be attributed to IMF conditions where B_y and B_z
 830 components are more dominant. Finally, assuming that ripples in the quasi-perpendicular
 831 bow shock (Johlander et al., 2016) are related to the jets generation mechanism, maybe
 832 the smaller amplitude and scales of these ripples can affect the jet properties. Specifi-
 833 cally, the smaller amplitude of Qperp ripples can create a geometry in which the Qperp
 834 jet undergoes a larger breaking compared to the case of the sharper (more inclined) tran-
 835 sitions of the ripples associated with Qpar jets. The different scales could also contribute
 836 to the short duration of the Qperp jets. The smaller scale ripples would benefit the for-
 837 mation of smaller flow structure than larger ones regarding their tangential size. In turn,
 838 when these flows meet MMS under some random angle, their measured duration would
 839 be significantly smaller.

840 To investigate the possibility of an observational bias, we examine the distributions
 841 of the solar wind velocities associated with and without jets. We find that indeed, on av-
 842 erage the associated solar wind velocities are much higher for the quasi-parallel jets ($\langle V_{SW,||} \rangle \approx$
 843 495 km/s) than for the quasi-perpendicular jets ($\langle V_{SW,\perp} \rangle \approx 400 \text{ km/s}$). The stan-
 844 dard deviations were found to be $\sigma_{||,Jets} = 96 \text{ km/s}$ and $\sigma_{\perp,Jets} = 46 \text{ km/s}$ respec-
 845 tively. To calculate the total solar wind distribution, we used eleven months containing
 846 long periods of magnetosheath and jet observations and calculated the average veloc-
 847 ity. These months are: 10–12/2015 - 1, 2, 11, 12/2016 - 1, 2, 12/2017 and 1/2019, and
 848 contained 87% of the jets. The separation between quasi-parallel and quasi-perpendicular
 849 was done based on the cone angle being lower or higher than 45 degrees. when observ-
 850 ing the total solar wind distribution, solar wind velocities associated with the Qperp bow
 851 shock ($\langle V_{SW,\perp} \rangle \approx 421 \text{ km/s}$) have a smaller difference to the solar wind velocities as-
 852 sociated with Qpar bow shock ($\langle V_{SW,||} \rangle \approx 444 \text{ km/s}$). The standard deviation are found
 853 to be $\sigma_{||} = 100 \text{ km/s}$ and $\sigma_{\perp} = 101 \text{ km/s}$ respectively. As a result, while the differ-
 854 ence of the solar wind conditions associated to jets is around $\sim 100 \text{ km/s}$, for the so-
 855 lar wind, it is only $\sim 20 \text{ km/s}$. It should be noted that, the difference between the Qpar
 856 and Qperp solar wind is smaller than one standard deviation. Therefore it is statistically
 857 unlikely that it is the effect contributing the most.

858 From the discussion above, we can conclude that all four effects (absence of SLAMS,
 859 observational bias, differences in SW, smaller scale ripples) could in principle take place
 860 and contribute to the differences that were observed between the jet properties of Qpar
 861 and Qperp jets.

862 The distance from the bow shock appears to be different for quasi-parallel and quasi-
 863 perpendicular jets, with Qpar jets occurring on average closer to the bow shock than Qperp
 864 jets. It should be noted, that this result might be artificial since (as discussed above) Qperp
 865 jets are found more frequently during low solar wind dynamic pressure conditions, which
 866 affects the positions of the bow shock and the magnetopause. As a result, when MMS
 867 measures a Qperp jet it will be further away from the bow shock and closer to the mag-
 868 netopause than a Qpar jet found in the same position. To quantify this effect, we used
 869 the average conditions found in the solar wind when Qpar and Qperp jets were observed
 870 and derived a model for the magnetopause and the bow shock. It was found that the av-
 871 erage standoff distance for the bow shock is $R_{0,BS,||} = 14.8 R_E$ for the Qpar jets and
 872 $R_{0,BS,\perp} = 15.3 R_E$ for the Qperp jets. This difference can explain Figure 5. This was
 873 expected since in Figure 6, it was already shown that the average position of MMS for
 874 both classes is the same. Furthermore, by performing the same procedure for the mag-
 875 netopause standoff distance, it was found that the average standoff distance is $R_{0,MP,||} =$
 876 $10.0 R_E$ for the Qpar jets and $R_{0,MP,\perp} = 10.9 R_E$ for the Qperp jets. Once more, this
 877 can explain the results shown regarding the magnetopause distance in Figure 6. It should
 878 be noted that modeling the bow shock under the typical Qperp SW conditions (very low
 879 dynamic pressure) is problematic since in such cases, BS models may overestimate the
 880 bow shock distance (Dmitriev et al., 2003). While currently we can compare the posi-
 881 tion of jets and justify the observed distributions we cannot draw strong conclusions re-

882 guarding the relative position of the classes. To do that, a normalization over the mag-
 883 netosheath regions covered by MMS is required. However, at this point the classifica-
 884 tion code has been only applied for the jet measurements. Therefore classified (Qpar and
 885 Qperp) magnetosheath observations are not yet available.

886 It should, however, be noted that while possibly affected by modeling issues, the
 887 Qperp jets are indeed found closer to the magnetopause and further away from the bow
 888 shock as shown in Figure 5 and 6. While at this point a conclusion regarding their na-
 889 ture cannot be drawn, it is possible that Qperp jets are connected to either small scale
 890 bow shock ripples or to FTEs that as reported in other studies (Archer & Horbury, 2013)
 891 have similar characteristics to Qperp jets shown in this work. While as mentioned above
 892 the bow shock ripple mechanism is consistent with our observations, some Qperp jets
 893 exhibit properties similar to FTEs. This include density decrease ($\sim 20\%$ of Qperp jets),
 894 Alfvénic velocities and southward IMF ($\sim 50\%$ of Qperp jets). As a result, it is possi-
 895 ble that the subset of Qperp jets include more than 1 distinct population with possibly
 896 different origin. A possible connection to FTEs is planned to be investigated in more de-
 897 tail in the near future.

898 Finally, Qperp jets have a velocity increase that is on average equally distributed
 899 between each velocity component (Figure 9) and more importantly, velocities of the Qperp
 900 jets seem to have a different angle compared to the background flow as shown in Fig-
 901 ure 10. This result could mean several things. One possibility would be that the observed
 902 subset of Qperp jets originating from low-velocity solar wind can have a specific, pre-
 903 determined velocity orientation. On the other hand, Qpar jets may also originate from
 904 a particularly high-velocity solar wind subset which has another distinct, yet different,
 905 velocity orientation. Another possible explanation is that Qperp jets have travelled a longer
 906 distance in the magnetosheath region compared to Qpar jet (see Figure 5) which could
 907 cause the Qperp jet to have a less distinct difference compared to the background mag-
 908 netosheath flow.

909 Qpar and Qperp jets exhibit differences regarding their beta values and how mag-
 910 netic and thermal pressure contribute to their properties. While a higher β is found in
 911 the Qpar jets, when subtracting the contribution of the background magnetosheath, an-
 912 other picture arises. Qpar jets have $\Delta\beta_{mean} < 0$, which means that the magnetic pres-
 913 sure is more important for the jets than for the surrounding magnetosheath. In Qperp
 914 jets, however, the jet has a $\Delta\beta_{mean} \sim 0$. Specifically, while the overall region (mag-
 915 netosheath) is basically dominated in both cases by gas dynamics ($\beta_{mean} > 1$), the Qpar
 916 jets are maybe controlled relatively more by magnetic pressure and the Qperp jets are
 917 governed slightly more by thermal pressure.

918 These changes in β parameter can be interpreted via three different mechanisms.
 919 First of all, SLAMS originating from the ion foreshock increase the magnetic field of Qpar
 920 jets and create an initial increase in the magnetic pressure compared to the Qperp cases
 921 where SLAMS are absent. Secondly, the background magnetosheath regions have dif-
 922 ferences in density, temperature and possibly magnetic field, which could contribute to
 923 different results both in their total β parameter but also when subtracting the background
 924 ($\Delta\beta$). Finally, If we assume that Qperp jets indeed travel longer distances from the bow
 925 shock than Qpar jets, the differences in β might provide insight regarding the fate of the
 926 jets as they travel in the magnetosheath. Qperp jets are created further away and may
 927 have reached a later stage of their existence in which the magnetosheath background flow
 928 and the jet are guided equally by the gas dynamics and the background magnetic field.
 929 In this case, the weaker Qperp jets are maybe seen in a later stage of their magnetosheath
 930 propagation in which their already weak properties make them relatively insignificant
 931 to the magnetospheric environment.

932

5.2 Quasi-Parallel and Boundary Jets

933

934

935

936

937

938

939

940

941

942

943

944

945

946

947

As for the boundary jets, we did not find any significant differences in their properties compared to Qpar jets, indicating a very similar phenomenon. Although some differences can be observed between the two classes, almost all of them can be attributed to the different properties of the background magnetosheath before and after the jet. Specifically, for the boundary jets, by definition, the plasma surrounding them is of both Qpar and Qperp nature. Some authors have speculated that maybe boundary jets are driven primarily by magnetic field tension forces and therefore point to a different origin than the rest of the classes (Archer et al., 2012; Karlsson et al., 2018). However, our results clearly show, both the magnetic field components (Figure 5) and the magnetic field rotation angles (see Figure 10) being very similar to the quasi-parallel jets. Also, all their basic properties are almost identical. Their dynamic pressure and its components have very similar distributions and average values to these of Qpar jets (see Figure 4). The temperature and the magnetic field profiles along with their distance from bow shock are also alike (see Figures 5 & 7). Moreover, the correlations between the different quantities were very similar to the ones found in Qpar jets.

948

949

950

951

952

953

We, therefore, suggest that Qpar and boundary jets form a superset of jets with very similar properties and possibly the same origin. It is unlikely that different physical mechanisms may generate two subsets of jets with so similar statistical properties. One of the things that was not tested however, is how frequent these jets occur compared to how often we exhibit a switch between Qpar and Qperp magnetosheath. A detailed analysis of that could point out a frequency difference if any.

954

955

956

957

958

959

To summarize, our results suggest that the quasi-parallel and the boundary jets are the classes connected to jet-related phenomena, such as the throat aurora (Han et al., 2017; Wang et al., 2018), magnetopause reconnection (Hietala et al., 2018) and possibly the radiation belts (Turner et al., 2012; Xiang et al., 2016). Finally, both Qpar and boundary jets exhibit high earthward velocities and duration, making them important to investigate magnetosphere coupling phenomena and geoeffective properties.

960

5.3 Encapsulated Jets

961

962

963

From the observations of the encapsulated jets, we can infer that there are at least two distinct subgroups of jets that are perhaps associated to a different formation mechanism.

964

965

966

967

968

969

970

The first ones are those that exhibit a positive V_x or that have an extremely small velocity, $|V_x| < 20$ km/s (Figure 9, top left). These rare cases (7/57) could be the result of a plasma reflection from the magnetopause (e.g. (Shue et al., 2009)). This picture is also consistent with the general trend that encapsulated jets are found closer to the magnetopause than the rest of the jets, and could also explain why some of the jets have positive V_x since these reflected flows could in principle point to any direction when measured by MMS at any point of their lifetime.

971

972

973

974

975

976

977

978

979

980

For the encapsulated jets that have a strong enough negative V_x (50/57), a possible scenario is that they are associated with a rotation of the IMF, generating a Qpar and a Qperp plasma environment sequentially. The jet is created in the quasi-parallel plasma environment, having a higher velocity, it gradually overtakes the quasi-perpendicular plasma allowing the formation of a region of Qpar plasma 'encapsulated' within the Qperp magnetosheath plasma to be measured by MMS. Another explanation of the encapsulated jets' statistical properties is that some of them are FTE events, connected to reconnection events occurring at the magnetopause. Structures with similar properties have been suggested to be FTEs (e.g. (Bosqued et al., 2001; Phan et al., 2004; S. M. Petrinec et al., 2020)) and it is possible that part of their set corresponds to such events. This

981 could also explain the strong velocity components in the z and y direction that could re-
982 sult from the outflow region of such events.

983 Another possible explanation which we propose as the main hypothesis is that the
984 majority of encapsulated jets are a subset of quasi-parallel jets, created at the flanks of
985 the bow shock. This picture provides a direct explanation to the similarities that are gen-
986 erally found between Qpar and encapsulated jets (high velocity increase, low tempera-
987 ture anisotropy, distinct high energy ion population, etc.). After investigating the as-
988 sociated solar wind conditions it was found that encapsulated jets appear when the IMF
989 is dominated by a y component. This would result in a quasi-perpendicular bow shock
990 close to the subsolar region of the magnetosheath. At the same time, an ion foreshock
991 is formed in the flanks allowing the same effects that apply to Qpar jets to take place.
992 This picture allows a mechanism similarly described to the bow shock ripple mechanism
993 (Hietala et al., 2009; Hietala & Plaschke, 2013) to generate jets. We hypothesize that
994 the orientation of the normal vector ($\hat{\mathbf{n}}$) close to the flanks, can deflect the downstream
995 flow into a higher yz velocity component. Then one can speculate that other effects (e.g.
996 local magnetic field deformation, slingshot effects, etc.) cause a dominant yz velocity com-
997 ponent to be achieved. Finally, the definition we used for encapsulated jets, to be Qpar
998 plasma surrounded by Qperp, creates an observational bias, since in the case that en-
999 capsulated jets remain in quasi-parallel environment, they would simply be classified as
1000 Qpar jets.

1001 As a result, we believe that encapsulated jets are quasi-parallel jets generated at
1002 the flanks, that travel a long distance and are finally measured by MMS in quasi-perpendicular
1003 background magnetosheath. This hypothesis is illustrated in Figure 13.

1004 The presented hypothesis also explains how a few encapsulated jets exhibit veloc-
1005 ities higher than the upstream solar wind conditions associated to them. First, we have
1006 an error at the propagation of solar wind measurements to the bow shock. The data we
1007 are using are propagated to the bow shock nose and as a result, there is a time lag er-
1008 ror for the solar wind that arrives at the flanks of the bow shock. Secondly, such a jet,
1009 originating from the flanks of the bow shock, would take a long time to reach the ob-
1010 servation point (MMS). As a result, the solar wind measurement association done for each
1011 jet is more unreliable for these cases. It should be noted that while this hypothesis could
1012 explain the majority of the encapsulated jets, it may not apply for all of them.

1013 None of the presented mechanism can directly explain why encapsulated jets have
1014 a density distribution similar to the quasi-perpendicular jets. In Figure 4 we can see that
1015 there is little to no density increase within an encapsulated jet. This effect can be seen
1016 more clearly when calculating the difference of the mean density for the jet ($\Delta n = \langle n \rangle_{jet} -$
1017 $\langle n \rangle_{5min}$). Doing so we find that on average there is a density decrease in an encapsu-
1018 lated jet ($\Delta n_{mean} = -1.7 \text{ cm}^{-3} \text{ nPa}$). This is also supported by the distribution of the
1019 relative difference in velocity and density that can be seen in Figure 11 and in Table 4.
1020 here, we see several encapsulated jets showing a density decrease.

1021 One mechanism that can explain the density decrease is if expansion takes place
1022 while the jet travels through the magnetosheath region. This could also help to explain
1023 the difference of the densities found in Qperp jets that are also found at larger distances
1024 from the bow shock. To investigate this hypothesis, we search for correlations between
1025 the radial (R) distance from the bow shock origin point, and the difference in maximum
1026 density (Δn_{max}). Doing so for the subsolar jets ($n = 289$), it was found that they are
1027 moderately anti-correlated, $\rho_{Sp,subsolar} = -0.5 \pm 0.05$. It should be noted that this ef-
1028 fect remained when looking at class-specific correlations for the case of subsolar Qpar
1029 jets ($\rho_{Sp,subsolar,||} = -0.27$). For the rest of the classes, the sample size of subsolar jets
1030 was too small to derive any meaningful results. These results could possibly be inter-
1031 preted as a weak indication of expansion taking place while the jets travel in the mag-

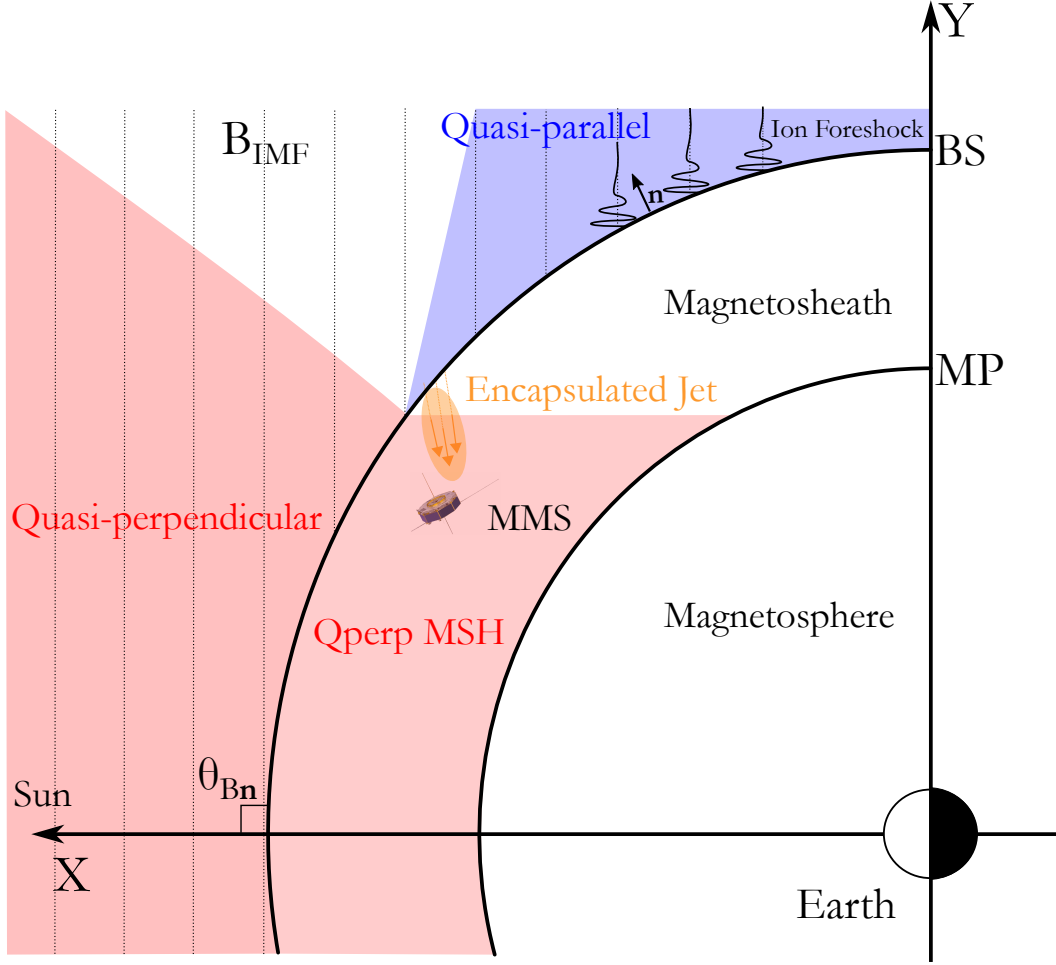


Figure 13. Visualization of encapsulated jet generation model. We assume a purely y component IMF which creates a large region of quasi-perpendicular angles around the subsolar point while the flanks are of quasi-parallel nature. The formation of the jet is done at the flanks of bow shock where ion foreshock is generated. Sequentially, MMS measures the jet travelling from the flanks towards the subsolar point, while the surrounding plasma is characterized by a constant flow originating from the quasi-perpendicular bow shock (red shaded area).

1032 netosheath region, although for drawing any stronger conclusions more in-depth anal-
 1033 ysis is required.

1034 Another possibility could be that a diffusion process due to magnetic reconnection
 1035 or Kelvin-Helmholtz instabilities at the boundary between the jet and the background
 1036 flow occurs, reducing the density of the jet as it travels in the magnetosheath.

1037 To summarize, the encapsulated jets are found on average further away from the
 1038 bow shock, they have on average a very large velocity in the yz plane while they usu-
 1039 ally exhibit a density drop. Their exact nature still needs to be determined. If their ori-
 1040 gin is associated to the bow shock and not other magnetospheric related events, they can
 1041 provide vital information regarding the evolution of the jet since we hypothesize that they
 1042 are flows that while having a high velocity they have undergone an expansion that low-
 1043 ers their density compared to Qpar jets. As a result, such a jet, if created at the flank
 1044 of the bow shock, it could create a very interesting case study to investigate the dynamic

1045 evolution of its properties from its formation at the bow shock until its observation. How-
 1046 ever, a possible connection to FTEs could also explain such observations since these jets
 1047 are occurring close to the magnetopause as shown in Figure 7. A more systematic anal-
 1048 ysis of these events is required in order to determine the exact nature of this subset of
 1049 jets.

1050 5.4 Generation Mechanisms of Jets

1051 As mentioned in the previous subsections, the bow shock ripple mechanism (Hietala
 1052 et al., 2009; Hietala & Plaschke, 2013) is supported indirectly by Figure 7 where we can
 1053 see that the difference between the temperature of the jet and the background is neg-
 1054 ative ($\Delta T < 0$) in Qpar jets, indicating that the jet flow could be less decelerated than
 1055 the background flow by passing through a bow shock ripple. Furthermore, in Figure 12(b,d),
 1056 it was shown that there is a moderate correlation between the maximum velocity dif-
 1057 ference and the minimum temperature difference. However, it is very hard to draw any
 1058 conclusion since the correlations are not robust enough. Although it seems that jet gen-
 1059 eration could be related to the ripples of the bow shock, there could be more factors that
 1060 influence their generation that may or may not be connected to this mechanism. A more
 1061 direct way to evaluate the bow shock ripple mechanism would be to analyze the jets that
 1062 appear close to the bow shock and compare with those found closer to the magnetopause.
 1063 Doing so, one can quantify how well the initial properties of the jets are explained through
 1064 the ripple mechanism and whether this effect gradually diminishes as the jets travel to-
 1065 wards the Earth. For the sake of completeness, we looked at jets close to the subsolar
 1066 point and to the bow shock and we found that the anti-correlation increases ($\rho_{Sp,subsolar} \approx$
 1067 -0.65 ± 0.1). However, more careful analysis is needed to investigate this effect, and
 1068 is planned to be done in future studies.

1069 We find support for the SLAMS-related mechanism (Karlsson et al., 2015) when
 1070 looking at the differences of maximum magnetic pressure (Figure 8) and most impor-
 1071 tantly at the correlations shown in Figure 12(a,c) between Δn_{max} and $\Delta |B|_{max}$. We con-
 1072 clude that SLAMS play an important role in contributing to the dynamic pressure en-
 1073 hancement of some of the Qpar jets. This can explain some of the differences in the prop-
 1074 erties of Qperp jets where SLAMS do not occur since they are a phenomenon typically
 1075 associated with the quasi-parallel bow shock.

1076 Both the bow shock ripple and SLAMS-associated mechanisms are therefore sup-
 1077 ported and appear to be key elements of jet formation. However, it could be the case
 1078 that there are more contributing mechanisms to the formation and composition of jets.
 1079 As previously discussed, the magnetic field is quite different for each class, while it is per-
 1080 sistentlly correlated to several basic properties of most jets. It is possible that the IMF
 1081 frozen into the solar wind has a more important impact on the jets than previously thought.
 1082 The high variance of the magnetic field shown in various jets could indicate instabilities
 1083 and wave activity that may play a role in establishing the jet properties. We believe that
 1084 more careful investigation regarding phenomena such as acceleration mechanisms, insta-
 1085 bilities, and wave interactions might lead to a more complete answer regarding the ori-
 1086 gin of the jets.

1087 Finally, there have been several cases where the correlations shown in all the jets
 1088 disappear when investigating class-specific correlations. This can be interpreted as a val-
 1089 idation of the classification, showing that the derived classes indeed represent a very sim-
 1090 ilar yet distinct physical phenomenon. However, it also indicates that, on large scale statis-
 1091 tics that include phenomena of diverse nature, correlation-driven conclusions can be un-
 1092 reliable and require further investigation. With the use of advanced techniques originat-
 1093 ing from probability and information theory (e.g. mutual information) along with care-
 1094 ful classification, sampling, and interpretation, we might in the future be able to derive
 1095 stronger conclusions regarding the origin and generation of jets.

1096

Appendix A Classification Thresholds and Stages

1097

For the classification process we use the following physical quantities:

$$\text{Averaged "very high" ion differential energy flux} \quad F_{VH} = \frac{1}{3} \sum_i^{30:32} F_i \quad (\text{A1a})$$

$$\text{Averaged "high" ion differential energy flux} \quad F_H = \frac{1}{3} \sum_i^{27:29} F_i \quad (\text{A1b})$$

$$\text{Averaged "medium" ion differential energy flux} \quad F_M = \frac{1}{5} \sum_i^{18:22} F_i \quad (\text{A1c})$$

$$\text{Summed magnetic field standard deviation} \quad \sigma(\mathbf{B}) = \sum_j^{1:3} \sigma(B_j) \quad (\text{A1d})$$

$$\text{Ion temperature anisotropy} \quad Q = \frac{T_{\perp}}{T_{\parallel}} - 1 \quad (\text{A1e})$$

$$\text{Total high / medium energy flux ratio} \quad C = \frac{F_{VH} + F_H}{F_M} \quad (\text{A1f})$$

1098

1099

1100

1101

1102

1103

1104

1105

where, i is the energy channel of the ion energy spectrum and j is the component of the magnetic field in GSE coordinates. We choose to not multiply with the energy difference (ΔE) for every bin of the energy flux in order to avoid weighting each flux component differently when averaging over. Very high energy flux represents ions of 16 – 28 keV, high energy is of 7 – 12 keV and medium is between 0.55 and 1.7 keV. More information regarding each energy bin can be found by accessing the MMS file repository (<https://lasp.colorado.edu/mms/sdc/public/about/browse-wrapper/>)

1106

1107

1108

1109

1110

1111

1112

1113

1114

1115

The classification process holds several stages, thresholds, and methods. In principle, the thresholds of each quantity are varied according to the values shown in Table A1. It should be noted that not all the thresholds have to be met in order for a classification to be made. Necessary criteria include F_{VH} , F_H , and $\sigma(\vec{B})$, while the others serve mainly as quality indicators and were used only for the classes of Qpar and Qperp jets. Furthermore, the actual classification is being done by separating the jet into three periods as explained in the main text (pre-jet, jet, post-jet). Then we apply these thresholds and classify each period depending on the class of the majority of the data points. During each stage, we vary the time period of pre-jet and post-jet slightly in order to allow the algorithm to take into consideration the different time scales that can occur for every jet.

1116

1117

1118

1119

1120

A simplified flowchart is shown in Figure A1, while a more detailed one can be found in the supplementary material. Figure A1 describes the algorithm after the initial clean up of jets is being done. Jets that are found very close to a bow shock crossing or that contain missing data within their pre/post jet time are not included in the classification algorithm.

1121

1122

1123

1124

1125

1126

1127

1128

1129

As shown in Figure A1, in stage 1 the jet is classified without any iterative process and by using the thresholds found in Table A1. If a jet does not get classified into one of the main classes it is moved to stage 2. In this stage, the algorithm varies the pre/post jet time for a number of tries to take under consideration possible differences between each jet. There are two kinds of variations that we utilize. First, we change the position of the pre and post jet periods to be further away from the jet. Then, we slightly increase the period of time that is initialized as described in Eq. 5. The next stages take the remaining unclassified jets and change the time average window along with the thresholds (Table A1) while again varying the pre/post jet times. At this point, the routine final-

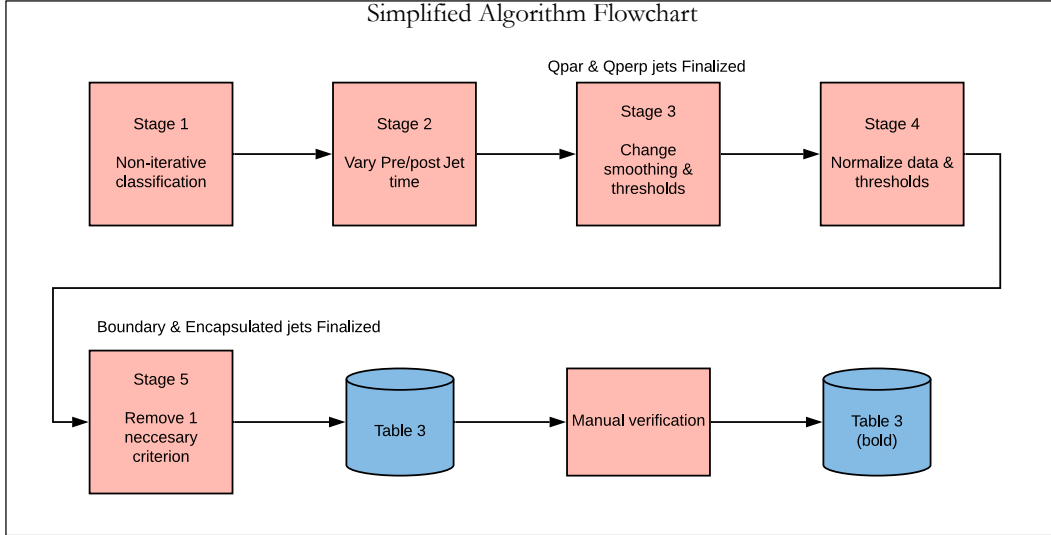


Figure A1. Simplified flowchart of the classification algorithm utilized to generate the dataset shown in Table 3.

1130 izes the Qpar and Qperp classes that are shown in Table 3. Moving on to stage 4, the
 1131 algorithm identifies potential boundary and encapsulated jets by normalizing the data
 1132 and using relative thresholds for the classification. The last stage removes one criterion
 1133 (F_H) in order to allow more jets to be classified to increase the sample size. This stages
 1134 finalizes the non-emphasized list shown in Table 3. The last step is to manually verify
 1135 the cases and determine if certain misclassifications occurred, this results in the empha-
 1136 sized (bold) cases shown in Table 3, that are called "final cases". More information re-
 1137 garding the exact procedure can be found in the supplementary material.

1138 **Appendix B Verification Procedure - Fine Parameter Searching**

1139 In order to verify the accuracy of the classification scheme, we created a test set
 1140 of 180 jets (identified by visual inspection) that represent the 4 main classes as shown
 1141 in Table 2, or that has been categorized as "unclassified". This set has been thoroughly
 1142 checked by visual inspection in order to represent a characteristic sample of the desired
 1143 classes that we are looking to classify.

1144 To create an initial classification scheme, some coarse threshold values and techni-
 1145 ques are implemented which we evaluated using the manually derived test set in order
 1146 to quantify the accuracy and the misclassification ratio of the code. The first accu-
 1147 racy results can be seen in Table B1.

1148 Accuracy is defined as the percentage of correct classifications. Misclassification
 1149 is defined as the percentage of classifications that were incorrectly classified to another
 1150 main class. For example, if a Qpar jet (class 1) was classified as unknown (class 0), the
 1151 accuracy is reduced but the misclassification rate does not increase. On the other hand,
 1152 if it had been classified as one of the main classes (e.g. boundary (class 3)) then the mis-
 1153 classification percentage would increase accordingly.

1154 Based on these results, we adjusted the thresholds several times, slightly changed
 1155 the procedure and introduced 1 more stage. Then adjustments were made until a max-
 1156 imum value of accuracy and a minimum value of misclassifications were achieved. The
 1157 final result of the classification scheme regarding its accuracy can be seen in Table B2.

Table A1. Quantities and thresholds used for each stage of the classification procedure. Number in the subscript indicates the average time window in seconds used for each quantity. Prime quantities (X') indicate a re-scaling of the quantity (min-max normalization: ($X \in [0, 1]$)). Average quantities ($\langle X \rangle$), are computed starting from 1 minute before the jet up to 1 minute after. Finally, $\Gamma = 0.05$ representing a threshold barrier for the normalized quantities. The differential ion energy flux is given in ($\text{keV}/\text{cm}^3 \cdot \text{s} \cdot \text{sr} \cdot \text{keV}$) and the standard deviation of the magnetic field vector in (nT).

Stages	Quasi - Parallel	Quasi - Perpendicular
1, 2	$F_{VH,30} > 2.9 \cdot 10^5$ $F_{H,30} > 4 \cdot 10^5$ $\sigma(\vec{B})_{60} > 14$ $Q_{30} < 0.4$ $C > 0.1$	$F_{VH,30} < 2.6 \cdot 10^5$ $F_{H,30} < 3 \cdot 10^5$ $\sigma(\vec{B})_{60} < 13$ $Q_{30} > 0.45$ $C < 0.075$
3	$F_{VH,0} > 3.0 \cdot 10^5$ $F_{H,0} > 4.1 \cdot 10^5$ $\sigma(\vec{B})_{30} > 14$ $Q_0 < 0.3$	$F_{VH,0} < 2.5 \cdot 10^5$ $F_{H,0} < 2.9 \cdot 10^5$ $\sigma(\vec{B})_{30} < 12$ $Q_0 > 0.35$
4, 5	$F'_{VH,0} > \langle F'_{VH,0} \rangle + \Gamma$ $F'_{H,0} > \langle F'_{H,0} \rangle + \Gamma$ $\sigma(\vec{B})'_{30} > \langle \sigma(\vec{B})'_{30} \rangle + \Gamma$ $Q'_0 < \langle Q'_0 \rangle - \Gamma$	$F'_{VH,0} < \langle F'_{VH,0} \rangle - \Gamma$ $F'_{H,0} < \langle F'_{H,0} \rangle - \Gamma$ $\sigma(\vec{B})'_{30} < \langle \sigma(\vec{B})'_{30} \rangle - \Gamma$ $Q'_0 > \langle Q'_0 \rangle + \Gamma$

Table B1. Initial accuracy before fine parameter searching.

Stage	Q-Par (%)		Q-Perp (%)		Bound. (%)		Encaps. (%)		Unknown (%)
	Acc.	Mis.	Acc.	Mis.	Acc.	Mis.	Acc.	Mis.	Mis.
1	94.7	0	36.4	0	10.8	0	4	4	0
2	94.7	0	39.4	0	10.8	0	20	4	0
3	94.7	0	84.9	0	10.8	0	20	4	11.9
4	94.7	2.6	84.9	3.1	89.2	0	80	4	45.3

Table B2. Final accuracy after fine parameter searching & last modifications. Emphasized text shows the stages that were found to work ideally for each class.

Stage	QPar (%)		QPerp (%)		Bound. (%)		Encaps. (%)		Unknown (%)
	Acc.	Mis.	Acc.	Mis.	Acc.	Mis.	Acc.	Mis.	Mis.
1	100	0	36.4	0	13.5	0	4	4	0
2	100	0	39.4	0	13.5	0	24	4	2.4
3	100	0	90.9	0	13.5	0	24	4	11.9
4	100	0	90.9	0	89.2	0	76	4	26.2
5	100	0	90.9	0	91.9	0	80	4	26.2

1158 The best sample size and classification accuracy for Qpar and Qperp jets were ob-
 1159 tained at stage 3. As a result, these classes do not get classified in the later stages. Mov-
 1160 ing on, for the boundary and encapsulated jets due to the complexity of their structure,
 1161 all 5 stages are used.

1162 The final step was to manually verify the cases that were misclassified from the un-
 1163 derrepresented classes (boundary & encapsulated). After doing so, we found no signif-
 1164 icant difference between the characteristics of the automatically derived database and
 1165 the manually cleaned one. However, to ensure the scientific value of the results, we val-
 1166 idated the dataset via manual inspection for the cases that the accuracy results were lower
 1167 and the number of jets was limited (boundary & encapsulated). This process provided
 1168 the final dataset shown in Table 3, which was then used for the main analysis of this work.

1169 Acknowledgments

1170 We thank the MMS team for providing data and support [https://lasp.colorado.edu/](https://lasp.colorado.edu/mms/sdc/public/)
 1171 [mms/sdc/public/](https://lasp.colorado.edu/mms/sdc/public/). Furthermore, we acknowledge use of NASA/GSFC's Space Physics
 1172 Data Facility's OMNIWeb service, and OMNI data. OMNI High-resolution data are avail-
 1173 able through https://omniweb.gsfc.nasa.gov/form/omni_min.html. This work was
 1174 supported by Swedish National Space Agency (SNSA grant 90/17).

1175 The final database of jets can be found in the supplementary material or accessed
 1176 via zenodo data repository (Raptis et al., 2020).

1177 References

- 1178 Amata, E., Savin, S., Ambrosino, D., Bogdanova, Y., Marcucci, M., Romanov, S.,
 1179 & Skalsky, A. (2011). High kinetic energy density jets in the earth's magne-
 1180 tosheath: A case study. *Planetary and Space Science*, *59*(7), 482–494.
- 1181 Anderson, B. J., Fuselier, S. A., Gary, S. P., & Denton, R. E. (1994). Magnetic
 1182 spectral signatures in the earth's magnetosheath and plasma depletion layer.
 1183 *Journal of Geophysical Research: Space Physics*, *99*(A4), 5877–5891.
- 1184 Angelopoulos, V., Kennel, C., Coroniti, F., Pellat, R., Kivelson, M., Walker, R.,
 1185 ... Gosling, J. (1994). Statistical characteristics of bursty bulk flow events.
 1186 *Journal of Geophysical Research: Space Physics*, *99*(A11), 21257–21280.
- 1187 Archer, M., Hietala, H., Hartinger, M., Plaschke, F., & Angelopoulos, V. (2019). Di-
 1188 rect observations of a surface eigenmode of the dayside magnetopause. *Nature*
 1189 *communications*, *10*.
- 1190 Archer, M., & Horbury, T. (2013). Magnetosheath dynamic pressure enhancements:
 1191 occurrence and typical properties. In *Annales geophysicae* (Vol. 31, p. 319).
- 1192 Archer, M., Horbury, T., & Eastwood, J. (2012). Magnetosheath pressure pulses:
 1193 Generation downstream of the bow shock from solar wind discontinuities.
 1194 *Journal of Geophysical Research: Space Physics*, *117*(A5).
- 1195 Behlke, R., André, M., Buchert, S. C., Vaivads, A., Eriksson, A. I., Lucek, E. A.,
 1196 & Balogh, A. (2003). Multi-point electric field measurements of short large-
 1197 amplitude magnetic structures (slams) at the earth's quasi-parallel bow shock.
 1198 *Geophysical research letters*, *30*(4).
- 1199 Bosqued, J. M., Phan, T. D., Dandouras, I., Escoubet, C. P., Rème, H., Balogh,
 1200 A., ... Sauvaud, J.-A. (2001). Cluster observations of the high-latitude
 1201 magnetopause and cusp: initial results from the cis ion instruments. *An-*
 1202 *nales Geophysicae*, *19*(10/12), 1545–1566. Retrieved from [https://](https://www.ann-geophys.net/19/1545/2001/)
 1203 www.ann-geophys.net/19/1545/2001/ doi: 10.5194/angeo-19-1545-2001
- 1204 Burch, J., Moore, T., Torbert, R., & Giles, B. (2016). Magnetospheric multiscale
 1205 overview and science objectives. *Space Science Reviews*, *199*(1-4), 5–21.
- 1206 Case, N., & Wild, J. (2012). A statistical comparison of solar wind propagation de-
 1207 lays derived from multispacecraft techniques. *Journal of Geophysical Research:*

- 1208 *Space Physics*, 117(A2).
- 1209 Chao, J., Wu, D., Lin, C.-H., Yang, Y.-H., Wang, X., Kessel, M., ... Lepping, R.
1210 (2002). Models for the size and shape of the earth's magnetopause and bow
1211 shock. In *Cospar colloquia series* (Vol. 12, pp. 127–135).
- 1212 Chen, S.-H., Kivelson, M. G., Gosling, J. T., Walker, R. J., & Lazarus, A. J. (1993).
1213 Anomalous aspects of magnetosheath flow and of the shape and oscillations
1214 of the magnetopause during an interval of strongly northward interplanetary
1215 magnetic field. *Journal of Geophysical Research: Space Physics*, 98(A4), 5727–
1216 5742.
- 1217 Dmitriev, A. V., Chao, J. K., & Wu, D. J. (2003). Comparative study of bow shock
1218 models using wind and geotail observations. *Journal of Geophysical Research:
1219 Space Physics*, 108(A12). Retrieved from [https://agupubs.onlinelibrary](https://agupubs.onlinelibrary.wiley.com/doi/abs/10.1029/2003JA010027)
1220 [.wiley.com/doi/abs/10.1029/2003JA010027](https://agupubs.onlinelibrary.wiley.com/doi/abs/10.1029/2003JA010027) doi: 10.1029/2003JA010027
- 1221 Dmitriev, A. V., & Suvorova, A. V. (2012). Traveling magnetopause distortion
1222 related to a large-scale magnetosheath plasma jet: Themis and ground-based
1223 observations. *Journal of Geophysical Research: Space Physics*, 117(A8).
1224 Retrieved from [https://agupubs.onlinelibrary.wiley.com/doi/abs/](https://agupubs.onlinelibrary.wiley.com/doi/abs/10.1029/2011JA016861)
1225 [10.1029/2011JA016861](https://agupubs.onlinelibrary.wiley.com/doi/abs/10.1029/2011JA016861) doi: 10.1029/2011JA016861
- 1226 Dmitriev, A. V., & Suvorova, A. V. (2015). Large-scale jets in the magnetosheath
1227 and plasma penetration across the magnetopause: Themis observations. *Jour-
1228 nal of Geophysical Research: Space Physics*, 120(6), 4423–4437. Retrieved
1229 from [https://agupubs.onlinelibrary.wiley.com/doi/abs/10.1002/](https://agupubs.onlinelibrary.wiley.com/doi/abs/10.1002/2014JA020953)
1230 [2014JA020953](https://agupubs.onlinelibrary.wiley.com/doi/abs/10.1002/2014JA020953) doi: 10.1002/2014JA020953
- 1231 Edgington, E. S. (2011). Randomization tests. In M. Lovric (Ed.), *Internat-
1232 ional encyclopedia of statistical science* (pp. 1182–1183). Berlin, Heidelberg:
1233 Springer Berlin Heidelberg. Retrieved from [https://doi.org/10.1007/978-3-
1234 -642-04898-2_56](https://doi.org/10.1007/978-3-642-04898-2_56) doi: 10.1007/978-3-642-04898-2_56
- 1235 Formisano, V., & Hedgecock, P. (1973). Solar wind interaction with the earth's
1236 magnetic field: 3. on the earth's bow shock structure. *Journal of Geophysical
1237 Research*, 78(19), 3745–3760.
- 1238 Fuselier, S. A. (2013). Suprathermal ions upstream and downstream from the earth's
1239 bow shock. In *Solar wind sources of magnetospheric ultra-low-frequency waves*
1240 (p. 107–119). American Geophysical Union (AGU). Retrieved from [https://
1241 agupubs.onlinelibrary.wiley.com/doi/abs/10.1029/GM081p0107](https://agupubs.onlinelibrary.wiley.com/doi/abs/10.1029/GM081p0107) doi: 10
1242 .1029/GM081p0107
- 1243 Fuselier, S. A., Anderson, B. J., Gary, S. P., & Denton, R. E. (1994). Inverse corre-
1244 lations between the ion temperature anisotropy and plasma beta in the earth's
1245 quasi-parallel magnetosheath. *Journal of Geophysical Research: Space Physics*,
1246 99(A8), 14931–14936.
- 1247 Giacalone, J., & Jokipii, J. R. (2007). Magnetic field amplification by shocks in tur-
1248 bulent fluids. *The Astrophysical Journal Letters*, 663(1), L41.
- 1249 Gosling, J., Asbridge, J., Bame, S., Paschmann, G., & Sckopke, N. (1978). Observa-
1250 tions of two distinct populations of bow shock ions in the upstream solar wind.
1251 *Geophysical Research Letters*, 5(11), 957–960.
- 1252 Gunell, H., Wieser, G. S., Mella, M., Maggiolo, R., Nilsson, H., Darrouzet, F., ...
1253 others (2014). Waves in high-speed plasmoids in the magnetosheath and at the
1254 magnetopause. In *Annales geophysicae* (Vol. 32, pp. 991–1009).
- 1255 Gutynska, O., Sibeck, D., & Omidi, N. (2015). Magnetosheath plasma structures
1256 and their relation to foreshock processes. *Journal of Geophysical Research:
1257 Space Physics*, 120(9), 7687–7697.
- 1258 Han, D.-S., Hietala, H., Chen, X.-C., Nishimura, Y., Lyons, L. R., Liu, J.-J., ...
1259 Yang, H.-G. (2017). Observational properties of dayside throat aurora and
1260 implications on the possible generation mechanisms. *Journal of Geophysical
1261 Research: Space Physics*, 122(2), 1853–1870. doi: 10.1002/2016JA023394
- 1262 Hietala, H., Laitinen, T. V., Andréevová, K., Vainio, R., Vaivads, A., Palmroth, M., ...

- 1263 Rème, H. (2009). Supermagnetosonic jets behind a collisionless quasiparallel
1264 shock. *Physical review letters*, *103*(24), 245001.
- 1265 Hietala, H., Partamies, N., Laitinen, T. V., Clausen, L. B. N., Facskó, G., Vaivads,
1266 A., ... Lucek, E. A. (2012). Supermagnetosonic subsolar magnetosheath jets
1267 and their effects: from the solar wind to the ionospheric convection. *Annales*
1268 *Geophysicae*, *30*(1), 33–48. Retrieved from [https://www.ann-geophys.net/](https://www.ann-geophys.net/30/33/2012/)
1269 [30/33/2012/](https://www.ann-geophys.net/30/33/2012/) doi: 10.5194/angeo-30-33-2012
- 1270 Hietala, H., Phan, T., Angelopoulos, V., Oieroset, M., Archer, M., Karlsson, T., &
1271 Plaschke, F. (2018). In situ observations of a magnetosheath high-speed jet
1272 triggering magnetopause reconnection. *Geophysical Research Letters*, *45*(4),
1273 1732–1740.
- 1274 Hietala, H., & Plaschke, F. (2013). On the generation of magnetosheath high-speed
1275 jets by bow shock ripples. *Journal of Geophysical Research: Space Physics*,
1276 *118*(11), 7237–7245.
- 1277 Johlander, A., Schwartz, S. J., Vaivads, A., Khotyaintsev, Y. V., Gingell, I., Peng,
1278 I. B., ... Burch, J. L. (2016, Oct). Rippled quasiperpendicular shock ob-
1279 served by the magnetospheric multiscale spacecraft. *Phys. Rev. Lett.*,
1280 *117*, 165101. Retrieved from [https://link.aps.org/doi/10.1103/](https://link.aps.org/doi/10.1103/PhysRevLett.117.165101)
1281 [PhysRevLett.117.165101](https://link.aps.org/doi/10.1103/PhysRevLett.117.165101) doi: 10.1103/PhysRevLett.117.165101
- 1282 Karlsson, T., Brenning, N., Nilsson, H., Trotignon, J.-G., Vallières, X., & Facsko,
1283 G. (2012). Localized density enhancements in the magnetosheath: Three-
1284 dimensional morphology and possible importance for impulsive penetration.
1285 *Journal of Geophysical Research: Space Physics*, *117*(A3).
- 1286 Karlsson, T., Kullen, A., Liljeblad, E., Brenning, N., Nilsson, H., Gunell, H., &
1287 Hamrin, M. (2015). On the origin of magnetosheath plasmoids and their rela-
1288 tion to magnetosheath jets. *Journal of Geophysical Research: Space Physics*,
1289 *120*(9), 7390–7403.
- 1290 Karlsson, T., Plaschke, F., Hietala, H., Archer, M., Blanco-Cano, X., Kajdic, P., ...
1291 Gershman, D. J. (2018). Investigating the anatomy of magnetosheath jets-mms
1292 observations. In *Annales geophysicae*.
- 1293 King, J., & Papitashvili, N. (2005). Solar wind spatial scales in and comparisons
1294 of hourly wind and ace plasma and magnetic field data. *Journal of Geophysical*
1295 *Research: Space Physics*, *110*(A2).
- 1296 Lavraud, B., Borovsky, J., Ridley, A., Pogue, E., Thomsen, M., Rème, H., ... Lucek,
1297 E. (2007). Strong bulk plasma acceleration in earth's magnetosheath: A
1298 magnetic slingshot effect? *Geophysical Research Letters*, *34*(14).
- 1299 Lin, Y., Swift, D., & Lee, L. (1996). Simulation of pressure pulses in the bow shock
1300 and magnetosheath driven by variations in interplanetary magnetic field direc-
1301 tion. *Journal of Geophysical Research: Space Physics*, *101*(A12), 27251–27269.
- 1302 Luhmann, J., Russell, C., & Elphic, R. (1986). Spatial distributions of magnetic field
1303 fluctuations in the dayside magnetosheath. *Journal of Geophysical Research:*
1304 *Space Physics*, *91*(A2), 1711–1715.
- 1305 Mailyan, B., Munteanu, C., & Haaland, S. (2008). What is the best method to cal-
1306 culate the solar wind propagation delay? In *Annales geophysicae* (Vol. 26, pp.
1307 2383–2394).
- 1308 Merka, J., Szabo, A., Narock, T., King, J., Paularena, K., & Richardson, J. (2003).
1309 A comparison of imp 8 observed bow shock positions with model predictions.
1310 *Journal of Geophysical Research: Space Physics*, *108*(A2).
- 1311 Myers, J. L., Well, A. D., & Lorch Jr, R. F. (2013). *Research design and statistical*
1312 *analysis*. Routledge.
- 1313 Němeček, Z., Šafránková, J., Přech, L., Sibeck, D., Kokubun, S., & Mukai, T.
1314 (1998). Transient flux enhancements in the magnetosheath. *Geophysical*
1315 *research letters*, *25*(8), 1273–1276.
- 1316 Omid, N., Zhang, H., Sibeck, D., & Turner, D. (2013). Spontaneous hot flow
1317 anomalies at quasi-parallel shocks: 2. hybrid simulations. *Journal of Geophysi-*

- 1318 *cal Research: Space Physics*, 118(1), 173–180.
- 1319 Palmroth, M., Hietala, H., Plaschke, F., Archer, M., Karlsson, T., Blanco-Cano, X.,
1320 ... others (2018). Magnetosheath jet properties and evolution as determined by
1321 a global hybrid-vlasov simulation. In *Annales geophysicae*.
- 1322 Petrinec, S. (2013, 04). On the magnetic field configuration of the magne-
1323 tosheath. *Terrestrial, Atmospheric and Oceanic Sciences*, 24, 265. doi:
1324 10.3319/TAO.2012.10.17.02(SEC)
- 1325 Petrinec, S. M., Burch, J. L., Chandler, M., Farrugia, C. J., Fuselier, S. A., Giles,
1326 B. L., ... Zhao, C. (2020). Characteristics of minor ions and electrons in flux
1327 transfer events observed by the magnetospheric multiscale mission. *Journal of*
1328 *Geophysical Research: Space Physics*, n/a(n/a), e2020JA027778. Retrieved
1329 from [https://agupubs.onlinelibrary.wiley.com/doi/abs/10.1029/](https://agupubs.onlinelibrary.wiley.com/doi/abs/10.1029/2020JA027778)
1330 [2020JA027778](https://agupubs.onlinelibrary.wiley.com/doi/abs/10.1029/2020JA027778) (e2020JA027778 2020JA027778) doi: 10.1029/2020JA027778
- 1331 Phan, T. D., Dunlop, M. W., Paschmann, G., Klecker, B., Bosqued, J. M., Rème,
1332 H., ... Kistler, L. M. (2004). Cluster observations of continuous reconnec-
1333 tion at the magnetopause under steady interplanetary magnetic field condi-
1334 tions. *Annales Geophysicae*, 22(7), 2355–2367. Retrieved from [https://](https://www.ann-geophys.net/22/2355/2004/)
1335 www.ann-geophys.net/22/2355/2004/ doi: 10.5194/angeo-22-2355-2004
- 1336 Plaschke, F., & Glassmeier, K.-H. (2011). Properties of standing kruskal-
1337 schwarzschild-modes at the magnetopause. In *Annales geophysicae* (Vol. 29,
1338 pp. 1793–1807).
- 1339 Plaschke, F., & Hietala, H. (2018). Plasma flow patterns in and around magne-
1340 tosheath jets. In *Annales geophysicae* (Vol. 36, pp. 695–703).
- 1341 Plaschke, F., Hietala, H., Angelopoulos, V., et al. (2013). Anti-sunward high-speed
1342 jets in the subsolar magnetosheath. In *Annales geophysicae*.
- 1343 Plaschke, F., Hietala, H., Archer, M., Blanco-Cano, X., Kajdič, P., Karlsson, T., ...
1344 others (2018). Jets downstream of collisionless shocks. *Space Science Reviews*,
1345 214(5), 81.
- 1346 Pollock, C., Moore, T., Jacques, A., Burch, J., Gliese, U., Saito, Y., ... others (2016).
1347 Fast plasma investigation for magnetospheric multiscale. *Space Science Re-*
1348 *views*, 199(1-4), 331–406.
- 1349 Raptis, S., Karlsson, T., Plaschke, F., Kullen, A., & Lindqvist, P.-A. (2020, April).
1350 *Magnetosheath jets mms (5/2015 - 6/2019)*. Zenodo. Retrieved from [https://](https://doi.org/10.5281/zenodo.3739553)
1351 doi.org/10.5281/zenodo.3739553 doi: 10.5281/zenodo.3739553
- 1352 Retinò, A., Sundkvist, D., Vaivads, A., Mozer, F., André, M., & Owen, C. (2007).
1353 In situ evidence of magnetic reconnection in turbulent plasma. *Nature Physics*,
1354 3(4), 235.
- 1355 Russell, C., Anderson, B., Baumjohann, W., Bromund, K., Dearborn, D., Fischer,
1356 D., ... others (2016). The magnetospheric multiscale magnetometers. *Space*
1357 *Science Reviews*, 199(1-4), 189–256.
- 1358 Savin, S., Amata, E., Zelenyi, L., Budaev, V., Consolini, G., Treumann, R., ... others
1359 (2008). High energy jets in the earth’s magnetosheath: Implications for plasma
1360 dynamics and anomalous transport. *JETP letters*, 87(11), 593–599.
- 1361 Savin, S., Amata, E., Zelenyi, L., Lutsenko, V., Safrankova, J., Nemecek, Z., ... oth-
1362 ers (2012). Super fast plasma streams as drivers of transient and anomalous
1363 magnetospheric dynamics. In *Annales geophysicae* (Vol. 30, p. 1).
- 1364 Schwartz, S. J., & Burgess, D. (1991). Quasi-parallel shocks: A patchwork of three-
1365 dimensional structures. *Geophysical Research Letters*, 18(3), 373–376.
- 1366 Schwartz, S. J., Burgess, D., Wilkinson, W. P., Kessel, R. L., Dunlop, M., & Lühr,
1367 H. (1992). Observations of short large-amplitude magnetic structures at a
1368 quasi-parallel shock. *Journal of Geophysical Research: Space Physics*, 97(A4),
1369 4209–4227.
- 1370 Shue, J.-H., Chao, J.-K., Song, P., McFadden, J. P., Suvorova, A., Angelopoulos, V.,
1371 ... Plaschke, F. (2009). Anomalous magnetosheath flows and distorted subsolar
1372 magnetopause for radial interplanetary magnetic fields. *Geophysical Research*

- 1373 *Letters*, 36(18). Retrieved from [https://agupubs.onlinelibrary.wiley](https://agupubs.onlinelibrary.wiley.com/doi/abs/10.1029/2009GL039842)
1374 [.com/doi/abs/10.1029/2009GL039842](https://agupubs.onlinelibrary.wiley.com/doi/abs/10.1029/2009GL039842) doi: 10.1029/2009GL039842
- 1375 Stone, E. C., Frandsen, A., Mewaldt, R., Christian, E., Margolies, D., Ormes, J., &
1376 Snow, F. (1998a). The advanced composition explorer. *Space Science Reviews*,
1377 86(1-4), 1–22.
- 1378 Stone, E. C., Frandsen, A., Mewaldt, R., Christian, E., Margolies, D., Ormes, J., &
1379 Snow, F. (1998b). The advanced composition explorer. *Space Science Reviews*,
1380 86(1-4), 1–22.
- 1381 Turc, L., Fontaine, D., Savoini, P., Hietala, H., & Kilpua, E. K. J. (2013). A
1382 comparison of bow shock models with cluster observations during low alfvén
1383 mach number magnetic clouds. *Annales Geophysicae*, 31(6), 1011–1019.
1384 Retrieved from <https://www.ann-geophys.net/31/1011/2013/> doi:
1385 10.5194/angeo-31-1011-2013
- 1386 Turner, D. L., Shprits, Y., Hartinger, M., & Angelopoulos, V. (2012). Explaining
1387 sudden losses of outer radiation belt electrons during geomagnetic storms. *Nature*
1388 *Physics*, 8(3), 208.
- 1389 Vuorinen, L., Hietala, H., & Plaschke, F. (2019). Jets in the magnetosheath: Imf
1390 control of where they occur. In *Annales geophysicae* (Vol. 37, pp. 689–697).
- 1391 Wang, B., Nishimura, Y., Hietala, H., Lyons, L., Angelopoulos, V., Plaschke, F.,
1392 ... Weatherwax, A. (2018). Impacts of magnetosheath high-speed jets on
1393 the magnetosphere and ionosphere measured by optical imaging and satel-
1394 lite observations. *Journal of Geophysical Research: Space Physics*, 123(6),
1395 4879–4894.
- 1396 Wilson III, L. (2016). Low frequency waves at and upstream of collisionless shocks.
1397 *Low-frequency waves in space plasmas*, 269–291.
- 1398 Xiang, Z., Ni, B., Zhou, C., Zou, Z., Gu, X., Zhao, Z., ... others (2016). Multi-
1399 satellite simultaneous observations of magnetopause and atmospheric losses of
1400 radiation belt electrons during an intense solar wind dynamic pressure pulse.
1401 *Annales Geophysicae (Online)*, 34(LA-UR-15-27237).
- 1402 Zhang, H., Sibeck, D., Zong, Q.-G., Omid, N., Turner, D., & Clausen, L. (2013).
1403 Spontaneous hot flow anomalies at quasi-parallel shocks: 1. observations. *Jour-*
1404 *nal of Geophysical Research: Space Physics*, 118(6), 3357–3363.